IMPLEMENTATION AND ASSESSMENT OF MODERN SHOCK-CAPTURING SCHEMES FOR HYPERSONIC VISCOUS FLOWS

A THESIS SUBMITTED TO
THE GRADUATE SCHOOL OF NATURAL AND APPLIED SCIENCES
OF
MIDDLE EAST TECHNICAL UNIVERSITY

BY

ÇAĞATAY ŞAHİN

IN PARTIAL FULFILLMENT OF THE REQUIREMENTS
FOR
THE DEGREE OF MASTER OF SCIENCE
IN
MECHANICAL ENGINEERING

AUGUST 2022

Approval of the thesis:

IMPLEMENTATION AND ASSESSMENT OF MODERN SHOCK-CAPTURING SCHEMES FOR HYPERSONIC VISCOUS FLOWS

submitted by **ÇAĞATAY ŞAHİN** in partial fulfillment of the requirements for the degree of **Master of Science in Mechanical Engineering Department, Middle East Technical University** by,

Prof. Dr. Halil Kalıpçılar
Dean, Graduate School of **Natural and Applied Sciences** ____________

Prof. Dr. Mehmet Ali Sahir Arıkan
Head of Department, **Mechanical Engineering** ____________

Assist. Prof. Dr. Özgür Uğraş Baran
Supervisor, **Mechanical Engineering, METU** ____________

Assist. Prof. Dr. Hediye Atik
Co-supervisor, **Aerospace Engineering, Atılım University** ____________

Examining Committee Members:

Prof. Dr. Mehmet Metin Yavuz
Mechanical Engineering, METU ____________

Assist. Prof. Dr. Özgür Uğraş Baran
Mechanical Engineering, METU ____________

Assist. Prof. Dr. Ali Karakuş
Mechanical Engineering, METU ____________

Assist. Prof. Dr. Hediye Atik
Aerospace Engineering, Atılım University ____________

Assist. Prof. Dr. Onur Baş
Mechanical Engineering, TEDU ____________

Date:

I hereby declare that all information in this document has been obtained and presented in accordance with academic rules and ethical conduct. I also declare that, as required by these rules and conduct, I have fully cited and referenced all material and results that are not original to this work.

Name, Surname: ÇAĞATAY ŞAHİN

Signature :

ABSTRACT

IMPLEMENTATION AND ASSESSMENT OF MODERN SHOCK-CAPTURING SCHEMES FOR HYPERSONIC VISCOUS FLOWS

ŞAHİN, ÇAĞATAY
M.S., Department of Mechanical Engineering
Supervisor: Assist. Prof. Dr. Özgür Uğraş Baran
Co-Supervisor: Assist. Prof. Dr. Hediye Atik

August 2022, 75 pages

Spatially second order accurate Finite Volume Method (FVM) is the most preferred method in Computational Fluid Mechanics (CFD) with its acceptable results in short computation times. FVM's accuracy heavily relies on the particular numerical scheme with which the fluxes are evaluated. Despite the maturity of traditional flux schemes today, simulations of a viscous hypersonic flow are still challenging. Since these cases involve strong shock waves and viscous layers with non-linear gradients, appropriate shock capturing is necessary for robust and accurate solutions. In this thesis, modern shock-capturing schemes based on Liou's AUSM and Von Neumann and Richtmyer's artificial viscosity are studied and implemented in an in-house CFD solver. The accuracy and robustness of the implemented methods for viscous hypersonic flow problems are tested with well-known numerical experiments. The comparison of the obtained results with each other and experimental data in the literature is presented. The advantages and disadvantages of schemes among each other are identified.

Keywords: hypersonics, shock-capturing, CFD, FVM

ÖZ

HİPERSONİK VİSKOZ AKIŞLAR İÇİN MODERN ŞOK YAKALAMA ŞEMALARININ UYGULANMASI VE DEĞERLENDİRİLMESİ

ŞAHİN, ÇAĞATAY
Yüksek Lisans, Makina Mühendisliği Bölümü
Tez Yöneticisi: Dr. Öğr. Üyesi. Özgür Uğraş Baran
Ortak Tez Yöneticisi: Dr. Öğr. Üyesi. Hediye Atik

Ağustos 2022, 75 sayfa

Uzayda ikinci dereceden hassas Sonlu Hacim Yöntemi (SHM) kısa hesaplama sürelerinde kabul edilebilir sonuçları ile Hesaplamalı Akışkanlar Mekaniği'nde (HAD) en çok tercih edilen yöntemdir. SHM'nin doğruluğu, akıların hesaplamasında kullanılılan numerik şemaya büyük ölçüde bağlıdır. Günümüzde geleneksel akı şemalarının olgunluğuna rağmen, viskoz bir hipersonik akışın simülasyonları hala zorludur. Bu durumlar, güçlü şok dalgaları ve doğrusal olmayan gradyanlara sahip viskoz katmanlar içerdiğinden, gürbüz ve doğru çözümler için uygun şok yakalama yöntemlerinin kullanılması gereklidir. Bu tezde, Liou'nun AUSM şemasına ve Von Neumann ile Richtmyer'in yapay viskozitesine dayanan modern şok yakalama şemaları, incelenmiş ve bir özgün HAD çözücüsünde uygulanmıştır. Viskoz hipersonik akış problemleri için uygulanan yöntemlerin doğruluğu ve gürbüzlüğü, iyi bilinen sayısal deneylerle test edilmiştir. Elde edilen sonuçların birbirleriyle ve literatürdeki deneysel verilerle karşılaştırılması sunulmuştur. Şemaların birbirleri arasındaki avantaj ve dezavantajları belirlenmiştir.

Anahtar Kelimeler: hipersonik, şok dalgası yakalama, HAD, SHM

To my family

ACKNOWLEDGMENTS

First and foremost, I would like to express my deepest gratitude to my thesis supervisor Assist. Prof. Dr. Özgür Uğraş BARAN for his guidance, motivation and understanding throughout the thesis study. Working with him was such a joyful and educational process.

I would like to thank my colleagues Ertan DEMİRAL, Dr. Kamil ÖZDEN and Kıvanç ARSLAN for their valuable discussions, advices and encouragement.

I also would like to thank my friends Osman Emre DENİZ and Enes AKAY for their mental support and amusing friendship.

My deepest thanks go to my parents, who have always supported me throughout my life. Every accomplishment I have made in life has been due to you both. Without their love and trust the completion of this thesis would not have been possible.

TABLE OF CONTENTS

ABSTRACT v

ÖZ vii

ACKNOWLEDGMENTS x

TABLE OF CONTENTS xi

LIST OF TABLES xiv

LIST OF FIGURES xv

LIST OF SYMBOLS xx

CHAPTERS

1 INTRODUCTION 1

- 1.1 Numerical Solutions of Hypersonic Flows 1
  - 1.1.1 Hypersonic Flight 1
  - 1.1.2 CFD Challenges 3
  - 1.1.3 Shock-Capturing 5
- 1.2 Literature Survey 5
- 1.3 Motivation,Objective and Outline of the Thesis 8

2 GOVERNING EQUATIONS AND NUMERICAL METHOD 11

- 2.1 Governing Equations 11
- 2.2 Finite Volume Method (FVM) 13

2.3 Discretisation of Inviscid Fluxes 15

2.4 The Method of Godunov 16

2.4.1 Riemann Problem 16

2.4.2 Godunov Approach 18

2.4.3 Exact Solution of Riemann Problem 20

2.4.4 Approximate Riemann Solvers 22

2.4.4.1 Roe Flux 22

2.4.4.2 HLLC Flux 24

2.5 Flux Vector Splitting Methods 25

3 SHOCK-CAPTURING METHODS 27

3.1 AUSM-family Schemes 27

3.1.1 AUSM+up 29

3.1.2 SLAU and SLAU2 32

3.2 Artifical Viscosity Methods for Curing Numerical Instabilities 35

3.2.1 Rodionov's Artificial Viscosity Method 35

3.2.2 A Pressure Ratio Based Artificial Viscosity Method 37

3.3 CFD Solver 39

4 NUMERICAL EXPERIMENTS AND RESULTS 41

4.1 Hypersonic Inviscid Flow Over a Cylinder 41

4.1.1 Problem Set-Up 42

4.1.2 Results 46

4.2 Subsonic Flat Plate 49

4.2.1 Problem Set-Up 50

4.2.2 Results 51
4.3 Ballistic Rocket Geometry HB-2 53
4.3.1 Problem Set-Up 53
4.3.2 Results 60
5 CONCLUSION AND FUTURE WORK 67
5.1 Conclusions 67
5.2 Future Works 68
REFERENCES 71

APPENDICES

LIST OF TABLES

TABLES

Table 4.1 Uniform divisions of meshes with different aspect ratios. 44

Table 4.2 C_{AV} minimum calibrated values. 46

Table 4.3 Laminar flow conditions. 51

Table 4.4 Turbulent flow conditions 51

Table 4.5 Flow properties for simulations. 54

Table 4.6 Simulation parameters 58

LIST OF FIGURES

FIGURES

Figure 1.1 A concept vehicle hypersonic transport. [1] 2

Figure 1.2 Physical effects characteristic of hypersonic flow.[1] 3

Figure 1.3 Structure of the carbuncle phenomena (density contours around a cylinder).[2] 4

Figure 2.1 Example of two dimensional quadrilateral computational cell. . . 14

Figure 2.2 Sod's shock tube problem. 17

Figure 2.3 Structure of the Riemann problem solution for Euler equations.[3] 17

Figure 2.4 Possible wave patterns of the Riemann problem solution for Euler equations.[3] 18

Figure 2.5 Piecewise constant distribution.[4] 19

Figure 2.6 Reimann problem solution at interaces.[4] 20

Figure 2.7 Structure of the Riemann problem solution for the three-dimensional case.[3] 21

Figure 2.8 Wave model for the HLLC solver.[5] 24

Figure 2.9 Splitting of the flux for cell i.[3] 26

Figure 3.1 AUSM (Advection Upstream Splitting Method) family tree.[6] . 30

Figure 3.2 Illustration of the function h for cell i. 38

Figure 3.3 Pressure ratio based function g.[7] 38

Figure 4.1 Aspect ratio of grids.[8] 42

Figure 4.2 Solution domain with boundary conditions 43

Figure 4.3 Computational domain and solutions of 90-321 grid 44

Figure 4.4 Computational domain and solutions of 125-321 grid 45

Figure 4.5 Computational domain and solutions of 250-321 grid 45

Figure 4.6 Density contours of AUSM based methods 46

Figure 4.7 Density contours of RAV methods 47

Figure 4.8 Density contours of PRAV methods 47

Figure 4.9 Densities over the stagnation line. 48

Figure 4.10 Contours of Mach number and artificial viscosity,μ_{AV} 49

Figure 4.11 Solution domain with boundary conditions 50

Figure 4.12 Computational domain. 50

Figure 4.13 Non-dimensional velocity for the flat plate laminar boundary layer problem. 51

Figure 4.14 Wall skin frictions for the flat plate laminar boundary layer problem. 52

Figure 4.15 Wall skin frictions for the flat plate turbulent boundary layer problem. 52

Figure 4.16 HB-2 geometry.[9] 53

Figure 4.17 Axisymmetric domain with boundary conditions. 54

Figure 4.18 Axisymmetric computational domain. 55

Figure 4.19 Three-dimensional domain with boundary conditions. 55

Figure 4.20 Three-dimensional computational domain. 56

Figure 4.21 Prism layers. 56

Figure 4.22 Axial force for different number of cells. 57

Figure 4.23 Convergence history of three-dimensional analyses. 58

Figure 4.24 Convergence history of axisymmetric analyses. 59

Figure 4.25 μ_{AV} contours of artificial viscosity methods for Case-3. 60

Figure 4.26 Velocity profiles for the HB-2 boundary layer. 61

Figure 4.27 Pressure distribution prediction over model surface for Case-1. . 62

Figure 4.28 Pressure distribution prediction over model surface for Case-2. . 63

Figure 4.29 Pressure distribution prediction over model surface for Case-3. . 64

Figure 4.30 Heat transfer prediction over model surface for axisymmetric case. 65

LIST OF SYMBOLS

SYMBOLS

γ	ratio of specific heat coefficients
$\hat{A}$	flux jacobian matrix
λ	second viscosity coefficient
μ	dynamic viscosity coefficient
μ_{AV}	artificial viscosity
$\overrightarrow{F^{(c)}}$	convective flux
$\overrightarrow{F^{(p)}}$	pressure flux
$\overrightarrow{F_c}$	inviscid flux vector
$\overrightarrow{F_v}$	viscous flux vector
$\overrightarrow{F}$	flux vector
$\overrightarrow{n}$	face normal
$\overrightarrow{Q}$	conservative variables vector
$\overrightarrow{S}.$	control volume surface
$\overrightarrow{U}$	contravariant Velocity
$\overrightarrow{V}$	velocity vector with the components u, v, and w
ρ	density
σ_i	viscous stress
τ_{ij}	viscous shear stress

Ω	control volume
a	speed of sound
C_{AV}	artificial viscosity coefficient
E	total energy per unit mass
e	internal energy per unit mass
H	total enthalpy per unit mass
h	characteristic mesh size
k	conductivity coefficient
p	pressure
q	conservative variable
R	specific gas constant
Re	Reynolds number
T	temperature
t	time
$y+$	non-dimensional wall distance
M	Mach number

CHAPTER 1

INTRODUCTION

1.1 Numerical Solutions of Hypersonic Flows

With the explosive development of computational resources and algorithms in the past decades, computational methods have been an essential component of engineering design and analysis, especially in fluid dynamics applications. Of course, experimental measurements and empirical calculations will always have a role. But, compared to these methods, Computational Fluid Dynamics (CFD) offers significant advantages in terms of cost, test time, ease of use, and output data quality. Today, CFD methods have mature abilities to solve flow fields with sophisticated geometries and complex physical processes. However, despite these advances, simulations of a hypersonic flow are still challenging and have room for improvement.

1.1.1 Hypersonic Flight

Hypersonic flight means flying approximately at least five times faster than the speed of sound. Vehicles with this ability 1.1 can enable easy space missions, the rapid military response at long range, and faster commercial transport. Therefore, it has been an growing demand to design air vehicles capable of flying at hypersonic speeds. To create such vehicles, engineers need to understand the behaviors and properties of hypersonic flows around the aerodynamic bodies.

One of these properties is the presence of strong shock waves close to the body's surface in external flow. As a result of the high Mach number, these strong shock waves will result in extreme temperature, and also pressure jumps over the shock wave. The small part of the flow field between the bow shock and the surface is called the shock layer. For increasing Mach numbers, shock angles over bodies become smaller and smaller. Thus, shock waves tend to hug closely to the body geometry at hypersonic speeds, making the shock layer smaller. This situation leads to shock wave interactions with other flow phenomena as shown in Figure 1.2, such as secondary shocks and boundary layers.[10]

Figure 1.1: A concept vehicle hypersonic transport. [1]

A vast amount of kinetic energy, contained by the freestream of hypersonic flow, is transformed into heat by viscous effects within the boundary layer. As a result, increased temperature in the boundary layer results in a decrease in density and an increase in viscosity coefficient via Sutherland's law. These phenomena make the thickness of hypersonic boundary layers larger than low Mach numbers at the same Reynolds number. Because of the wide boundary layer flow, the outer inviscid flow changes considerably, and these changes in the inviscid flow, in turn, affect the boundary layer. This interaction between the viscous region and the outer inviscid flow is named hypersonic viscous interaction. These interactions can affect hypersonic vehicles' surface heat transfer and pressure distributions. Therefore, viscous interaction alter, lift and drag forces, and also stability characteristics.

High-temperature effects are another essential characteristic of hypersonic flow fields, which dominate flow properties. Viscous dissipation of the kinetic energy and strong shock transitions in hypersonic flows leads to high gas temperatures. The extreme temperature can cause dissociation and ionization within the air. Therefore, the gas no longer behaves as thermally and calorically perfect and must instead be considered chemically reacting. That high-temperature, chemically reacting flow can influence a hypersonic vehicle's aerodynamic forces and moments.

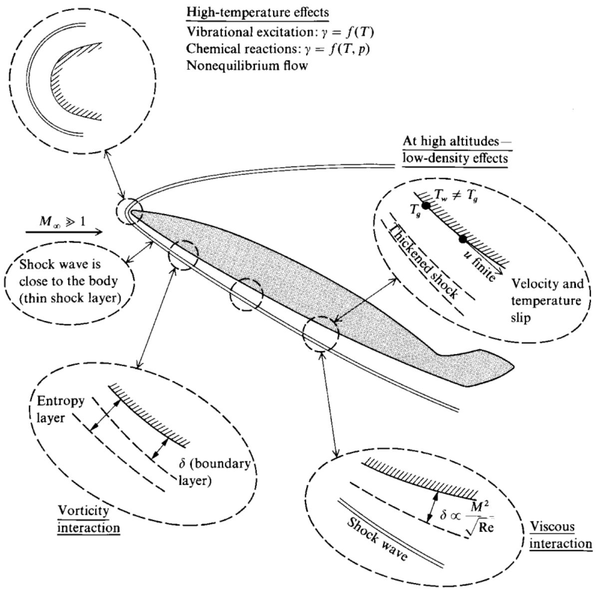

Figure 1.2: Physical effects characteristic of hypersonic flow.[1]

1.1.2 CFD Challenges

The complex physical phenomena in hypersonic flow make the development of numerical simulations very troublesome. Accurate prediction of heat transfer distribution on a surface is the main problem in hypersonic flow computations. However, even if we neglect chemical reactions and try to solve the flow domain with ideal gas assumption, it is still one of the toughest problems to solve in CFD. The calculation accuracy of heating prediction is closely connected to the computational mesh and numerical methods. Since there are huge variable jumps at shock waves and strong-nonlinear temperature and pressure distributions in the boundary layer, the mesh need to be dense and high quality in those regions. Also, the numerical scheme's robustness and accuracy are essential in accurate heating prediction. Low-dissipative, high-order numerical methods must be used to resolve this complex flow domain. However, due to the Gibbs phenomenon, which is the name of the oscillatory behavior of differentiable equations variables around discontinuities, solutions of these low-dissipative schemes suffer from shock anomalies (instabilities or oscillations), including the carbuncle phenomena.

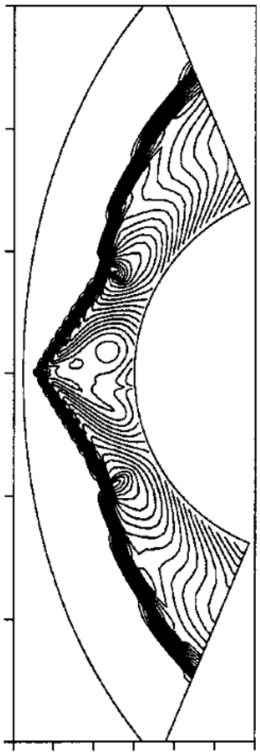

Figure 1.3: Structure of the carbuncle phenomena (density contours around a cylinder).[2]

The carbuncle phenomena is a numerical instability that forms as a tumor ahead of the bow shock along the stagnation line, as seen in Figure 1.3. In 1988, the carbuncle phenomena was first observed by Imlay and Peery[11]. They performed invisicid flow simulatons around a blunt body problem at hypersonic speeds. Their trial of capturing the bow shock with a low-dissipative scheme (Roe) resulted in a non-physical solution. Later, Quirk [12] revealed that the carbuncle phenomena could be triggered easily by low diffusion schemes designed to capture contact and shear discontinuities with minimal smearing. Also, he presented a list of problems with anomalous solutions. Quirk proposed a new test problem to examine whether a scheme is free from shock instability, called Quirk's test or Odd-even problem. This test corresponds to the unsteady flow problem in which a planar shock wave moves in a 1-D tube left to right. It became an efficient tool for diagnosing the schemes and revealing their susceptibility to the carbuncle flaw. These shock anomalies, particularly the carbuncle phenomena, can severely degrade the predictability of hypersonic heating since it is essential to understand and cure this instability problem.

1.1.3 Shock-Capturing

In non-linear hyperbolic problems, oscillations and wiggles occur near large gradients, like shock waves. This problem is known as the Gibbs phenomenon. The main idea behind eliminating these anomalies is to introduce numerical dissipation to the conservative governing equations. Dissipation enlarges the thickness of a shock from one to a few elements in the computational domain by smearing discontinuity. Therefore, strong discontinuity is replaced by thin transition layers, where flow variables change rapidly but continuously. By dividing a large gradient into smaller ones, we relax spurious oscillations at its front. This process is known as shock-capturing. But, this extra dissipation must be bounded near shock regions, mainly for viscous flow solutions. Otherwise, it can degrade the accuracy of the overall solution, especially in high gradient regions, such as boundary-layer. In summary, a numerical method suitable for the solution of flows that involve strong shock waves, like hypersonic ones, should be robust against the unphysical shock anomalies. Considering the discussions on the boundary layer interactions, these methods should simultaneously provide a high boundary-layer resolution.[13]

1.2 Literature Survey

Capturing strong shock waves is one of the primary research subjects of CFD. Since hypersonic flow solutions are very delicate to shock instabilities, like the carbuncle phenomena. Although many active efforts exist to generate high-order methods [10] for hypersonic flow solutions. Due to its robust and conservative performance, the finite volume method(FVM), which is spatially second-order accurate, is still generally used for these computations, especially in industrial applications. And in FVM, the method's performance heavily relies on shock-capturing methods used in the solution.

In 1950, Von Neumann and Richtmyer [14] proposed the first shock-capturing method. The method's main idea is introducing an artificial viscosity term into the governing equations to smear shock waves over several grids. Later, in 1954, Lax[15] introduced a simple scheme that obtains numerical flux by averaging the left and right states arithmetically(central differencing). The scheme, later called the Lax-Friedrichs or Rusanov method, could capture shock waves without adding artificial viscosity. Although, their method is simple, it is too dissipative.

In 1959, Godunov revealed his paper [16] which significantly impacted the further evolution of inviscid flux functions. He offered a method that relies on the solution of the Riemann problem for flux calculations. His approach demonstrated exceptional robustness, accuracy. Therefore, it became very popular after its discovery by western academia in the 80s, and many researchers employed his unique idea to solve Euler equations. These inviscid flux evaluation functions can be classified as Flux Vector Splitting (FVS) and Flux Difference Splitting (FDS) methods.

First FVS schemes, introduced by Steger&Warming [17] and Van Leer [18], are advantageous because of their high stability. This stability property, which stems from excessive numerical dissipation, makes them robust for simulations of high-speed flows involving strong shock waves and expansions. However, these methods are not recommended for viscous flows because of their poor boundary and shear layer resolution and inaccurate estimates of heat transfer rates.

Another approach, FDS schemes, which solve the Riemann problem for Euler equations approximately at the cell interfaces, can be generally classified into two groups as complete and incomplete Riemann solvers. The incomplete Riemann solvers, including the Harten-Lax-van Leer (HLL) scheme[19] and the Harten-Lax-van Leer-Einfeldt (HLLE) scheme[20], assume a wave structure consisting of two waves that separate three constant states. This assumption lead to excessive dissipation due to a lack of contact discontinuity. Thus these two methods also have high resistance to shock instabilities but they are unsuitable for viscous flow calculations like FVS schemes. On the opposite, complete Riemann solvers, like Roe [21] and HLL with contact (HLLC) [22], have the same wave structure (three-wave) as the exact Riemann problem solution and reveal minimal dissipation. Therefore, they are qualified for computing viscous flows. However, such schemes are very vulnerable to shock instabilities and carbuncle phenomena, which restrict their application range in hypersonic flows.

To solve this dilemma, many researchers have made tremendous efforts. Numerous methods have been proposed to enhance the CFD codes' performance of shock-capturing at high speeds. The general strategy for eliminating shock instabilities is introducing additional numerical dissipation in the vicinity of the shock waves. However, this dissipation must be minimized in regions like the stagnation and the boundary layer (low-speed areas) to resolve continuous variable gradients accurately. For years, to balance shock-capturing schemes between accuracy and robustness, three primary methodologies have been employed by researchers.

The first strategy to overcome the shock wave instabilities is switching to a complementary shock-stable scheme near shock waves and relative low-dissipative schemes elsewhere. Quirk [12] introduced the idea of hybridizing complementary Riemann solvers for high-speed flow calculations. His idea gathered much attention in the following years. Several scientists followed him and proposed their hybrid flux functions. For notable recent studies reader is referred to Wang's, Shen's and Xie's works [23, 24, 25]. These schemes combine a contact-shear wave preserving complete solver with an incomplete diffusive one. To switch between solvers, they used shock sensors. These sensors allow to determine the appropriate solver depending on the flow conditions encountered. While the diffusive scheme is employed near shock waves to suppress oscillations and instabilities, and the accurate solver is used to resolve the remaining regions. The switching function should be designed carefully to sustain the accuracy and robustness of schemes, especially for unstructured grids. Simon mentioned [26, 27, 28] that hybrid fluxes require complete evaluation of both flux functions, and they are generally computationally expensive to implement. Because of that, he chose to hybridize fluxes by adding diffusive components of incomplete solvers to complete ones to reduce the cost of functions.

Second approach is intoduced by NASA scientist Liou [29] in 1993. He identified dissipative pressure term in the mass flux is responsible for the instabilities of high-speed computations. With that discovery, he introduced a simple, robust and accurate approach for high-speed flow computations, which is called Advection Upstream Splitting Method (AUSM). Many AUSM scheme variants emerged since then, and they are categorized as AUSM-family schemes. These schemes are stable and also accurate by being able to capture contact discontinuities. This feature achieved by separating pressure-flux terms from the mass-flux based terms. Thus, they have been very popular for compressible flow applications. Liou also developed an all-speed extension [30] of the classical method, which is applicable from low to high Mach number flow solutions. However, this scheme, AUSM+up, has insufficient robustness and requires a user-defined parameter, the cut-off Mach number. This requirement also limits the usage of the scheme to internal flow problems. In recent years, to avoid the problem-dependent parameters of AUSM+up, Kitamura and Shima have introduced their all-speed AUSM scheme, SLAU(Simple Low-dissipative AUSM) [31]. However, SLAU is not robust enough for hypersonic flows and is not extendable to real gas flows. Thus, Kitamura further developed SLAU2 [32] which has good performance in hypersonic flow computations. Also, Kitamura tried to formulate HLLC in a very similar form to the AUSM scheme to combine the strengths of both flux functions. The resultant scheme, HLLC with low-dissipation scheme (HLLCL) [33] , is applicable to both low and high Mach number flows.

In 2017, Rodionov [34] proposed another approach for curing numerical instabilities in hypersonic flows. Differently from the hybrid methods, which use numerical dissipation inherent in inviscid flux functions to capture strong shock waves, he suggested adding explicit dissipation, which relies on Von Neumann and Richtmyer's [14] artificial viscosity to smear discontinuities. Rodionov's method introduces numerical dissipation in the form of the RHS of the Navier-Stokes equations. Since applied dissipation is independent of the combined flux function, it can be used to cure the shock instabilities with all Riemann solvers. In the following years, he proposed three improved versions of classical method [35, 36, 37] to expand the range of applications.

1.3 Motivation,Objective and Outline of the Thesis

As mentioned in the previous sections, robust and accurate hypersonic flow analysis is essential in the aerospace industry. Although there are lots active efforts to develop high-order methods, such as ENO, WENO, for hypersonic computations, spatially second order accurate FVM is the most preferred method in CFD with its acceptable results with significantly less computational costs. To ensure FVM's accuracy in high-speed flows, many shock-capturing schemes, which are robust against unphysical shock anomalies and capable of resolving gradients in low-speed regions, have been proposed in recent years.

The current shock capturing schemes has their stregths and weaknesses. Hybrid schemes are robust, but costly. AUSM family solvers solves many problems, but they are less accurate than some Riemann solvers. The artificial viscosity methods's parameters may be problem and mesh dependent. Therefore in this thesis our motivations are:

- Determine dissipative behaviours of common shock capturing schemes
- Propose a new method that combines the strength of Riemann based methods and artificial viscosity methods and show that this method can be applicable in a wide range of Mach numbers.

Therefore, this thesis aims to compare the performance of prominent shock-capturing methods in the literature in viscous high-speed flow computations. For that purpose, widely known AUSM+up, SLAU2 flux functions are explained and implemented into the in-house compressible flow solver, which already has HLLC and Roe. Furthermore, Rodinov's artificial viscosity approach is also investigated and added to the code. In addition, instead of Rodinov's shock detection sensor, a new pressure-ratio based sensor based on Chen's work [7] is suggested to tune artificial viscosity. The new approach removes the weaknesses of the Rodinov' method including mesh-dependent parameters. Several numerical experiments are conducted to assess implemented methods' performance in high-speed applications. Obtained results are compared with each other and the ones presented in the literature.

The main objective of this work is to compare the before-mentioned shock-capturing schemes with numerical experiments to understand the features inherited by each technique also their advantages and disadvantages. And by implementing them into the in-house FVM solver, enhancing its high-speed flow solution capability. The scope of this thesis is limited to ideal gases. Chemistry, radiation, and material ablation are not considered.

This thesis is organized as follows. Chapter 2 briefly reviews governing equations of viscous compressible flows and their related finite volume discretization. Godunov's method of solution and construction of traditional flux functions are also given in the same section. In chapter 3, the theory behind implemented shock-capturing methods is presented. Then, the accuracy and robustness of the proposed methods for hypersonic flow problems are tested with well-known test cases in Chapter 4. Finally, the conclusion and future works are presented in Chapter 5.

CHAPTER 2

GOVERNING EQUATIONS AND NUMERICAL METHOD

This chapter aims to describe the foundations on which this work is built. Firstly, governing equations for the compressible, viscous flow are presented in conservative form. Secondly, the finite volume discretization method and usage of compressible Euler equations for inviscid flux derivation are explained. Finally, the traditional methodologies for evaluating the inviscid fluxes are presented.

2.1 Governing Equations

Governing equations of viscous, heat conducting, compressible flow without any external body force or heat generation are known as Navier-Stokes equations. They are a system of non–linear equations, which consist of conservation of mass, momentum and energy [38][39]. The general form of the conservation equation states that the rate of change of total quantity q within the control volume Ω. In the absence of sources equation becomes

$$\frac{\partial}{\partial t}\int\limits_{\Omega} q d\Omega + \oint\limits_{S} \overrightarrow{F} \cdot d\overrightarrow{S} = 0 \tag{2.1}$$

where$\overrightarrow{F}$,flux vector of q, is the amount of the quantity crossing a unit surface per unit time and $\overrightarrow{S}$ is the face of the control volume. This integral form of conservation equation(2.1) is utilized to write three-dimensional Navier-Stokes equations in integral form as

$$\frac{\partial}{\partial t}\int_{\Omega}\overrightarrow{Q}d\Omega+\oint_{S}(\overrightarrow{F_c}-\overrightarrow{F_v})\cdot d\overrightarrow{S}=0 \tag{2.2}$$

$\overrightarrow{Q}$ represents the vector of conservative variables, while $\overrightarrow{F_c}$ is known as inviscid flux. Both vectors contain five cartesian components for three-dimensional case.

$$\overrightarrow{Q}=\begin{bmatrix}\rho\\ \rho u\\ \rho v\\ \rho w\\ \rho E\end{bmatrix},\overrightarrow{F_c}=\begin{bmatrix}\rho\\ \rho u\\ \rho v\\ \rho w\\ \rho E\end{bmatrix}U+\begin{bmatrix}0\\ n_x\\ n_y\\ n_z\\ \overrightarrow{V}\end{bmatrix}p \tag{2.3}$$

Where U is the contravariant velocity, that is the velocity normal to the surface element $d\overrightarrow{S}$. It can be defined as

$$U=\overrightarrow{V}\cdot\overrightarrow{n} \tag{2.4}$$

To describe the work of viscous stresses and the heat conduction in the fluid, vector of viscous fluxes $\overrightarrow{F_v}$ is defined as in equation (2.5)

$$\overrightarrow{F_v}=\begin{bmatrix}0\\ \tau_{xx}\hat{i}+\tau_{xy}\hat{j}+\tau_{xz}\hat{k}\\ \tau_{yx}\hat{i}+\tau_{yy}\hat{j}+\tau_{yz}\hat{k}\\ \tau_{zx}\hat{i}+\tau_{zy}\hat{j}+\tau_{zz}\hat{k}\\ (\sigma_x+k\frac{\partial T}{\partial x})\hat{i}+(\sigma_y+k\frac{\partial T}{\partial y})\hat{j}+(\sigma_z+\frac{\partial T}{\partial z})\hat{k}\end{bmatrix} \tag{2.5}$$

Shear stress terms can be formulated with second viscosity coefficient λ ,and the dynamic viscosity coefficient μ as follows.

$$\sigma_x=\tau_{xx}u+\tau_{xy}v+\tau_{xz}w \tag{2.6}$$

$$\sigma_y=\tau_{yx}u+\tau_{yy}v+\tau_{yz}w \tag{2.7}$$

$$\sigma_z = \tau_{zx}u + \tau_{zy}v + \tau_{zz}w \tag{2.8}$$

$$\tau_{xx} = \lambda(\frac{\partial u}{\partial x} + \frac{\partial v}{\partial y} + \frac{\partial w}{\partial z}) + 2\mu\frac{\partial u}{\partial x} \tag{2.9}$$

$$\tau_{yy} = \lambda(\frac{\partial u}{\partial x} + \frac{\partial v}{\partial y} + \frac{\partial w}{\partial z}) + 2\mu\frac{\partial v}{\partial y} \tag{2.10}$$

$$\tau_{zz} = \lambda(\frac{\partial u}{\partial x} + \frac{\partial v}{\partial y} + \frac{\partial w}{\partial z}) + 2\mu\frac{\partial w}{\partial z} \tag{2.11}$$

$$\tau_{xy} = \tau_{yx} = \mu(\frac{\partial u}{\partial y} + \frac{\partial v}{\partial x}) \tag{2.12}$$

$$\tau_{xz} = \tau_{zx} = \mu(\frac{\partial u}{\partial z} + \frac{\partial w}{\partial x}) \tag{2.13}$$

$$\tau_{yz} = \tau_{zy} = \mu(\frac{\partial v}{\partial z} + \frac{\partial w}{\partial y}) \tag{2.14}$$

Navier-Stokes equations are coupled and should be solved simultaneously. It's seen that, there are six primary flow variables, density ρ, pressure p, temperature T and three velocity components u, v, w. Therefore, in order to close the system of equations, it is necessary to constitute relations between fluid properties by an equation of state. In general, compressible flows are assumed to be perfect gas. The equation of state for a perfect gas can be written as in Equation 2.15.

$$p = \rho RT \tag{2.15}$$

2.2 Finite Volume Method (FVM)

The differential formulation of conservation laws assumes variables are sufficiently smooth in all solution domainsto allow the differentiation operation. On the other hand, the intgeral form indicates conservation laws in which the smooth change of variables assumption is relaxed to allow discontinuities in solution domains. Thus, problems, involving discontinuities such as shocks, must be solved by integral form of governing equations for accurate results.

The finite volume method is a discretization method, which divides the physical domain into arbitrary control volumes and applies the integral conservation laws to that local volume. Historically, it was introduced in CFD independently by Mc Donald [40] and MacCormack and Paullay [41]. The method relies upon the direct discretization of the integral form of the conservation laws. Thus, FVM obeys the physics of the compressible flow and allows solutions with discontinuities. It is the most preferred method today in CFD. The reasons for this are its generality, simple structure, and ease of implementation for arbitrary mesh, including both structured and unstructured grids.

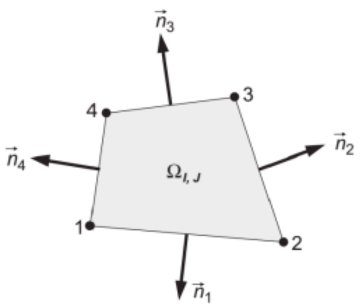

Figure 2.1: Example of two dimensional quadrilateral computational cell.

In FVM, the surface integral part of conservation equation (2.1) is approximated by the sum of the fluxes crossing the individual faces of the control volume. The conservation law for control volume given in Figure 2.1 can be defined as

$$\Omega_i \left(\frac{\partial \overrightarrow{q_i}}{\partial t} \right) + \sum_{j=1}^{4} \overrightarrow{F}_{ij} \cdot \overrightarrow{S}_{ij} = 0 \tag{2.16}$$

The key point of this formulation is the fact that the time variation of q inside the volume ,Ω_i, only change with the surface flux contributions. Thus, the accuracy of the method directly depends on the particular function with which the fluxes are evaluated. In Navier-Stokes equations, inviscid flux terms are related to the hyperbolic nature of the equations, whereas the viscous stress terms are related to the parabolic nature. Therefore, while viscous flux can be generally computed by a central difference, researchers have developed numerous different methods to obtain the inviscid flux through the cell interface.

2.3 Discretisation of Inviscid Fluxes

In general, the Euler equations describe the inviscid flows. Therefore, inviscid fluxes are approximated from the discretization of these conservation equations. In condensed notation Euler Equations can be written as in Equation (2.17).

$$\frac{\partial \overrightarrow{Q}}{\partial t} + \overrightarrow{\nabla} \cdot \overrightarrow{F} = 0 \tag{2.17}$$

where $\overrightarrow{Q}$,and $\overrightarrow{F}$ are same with Navier-Stokes equations.

$$\overrightarrow{Q} = \begin{bmatrix} \rho \\ \rho u \\ \rho v \\ \rho w \\ \rho E \end{bmatrix}, \overrightarrow{F} = \begin{bmatrix} \rho \\ \rho u \\ \rho v \\ \rho w \\ \rho E \end{bmatrix} U + \begin{bmatrix} 0 \\ \hat{i} \\ \hat{j} \\ \hat{k} \\ \overrightarrow{V} \end{bmatrix} p \tag{2.18}$$

These equations are hyperbolic type partial differential equations. They have directional and wavelike propagation characteristic. The inviscid flux terms are directly related to the hyperbolic nature of these equations. Therefore, numerical method for the evalutaion of inviscid fluxes must follow the physics of the flow and be consistent with the direction at which information propagates. For this reason, modern inviscid flux schemes are generally based on upwind discretizations, in opposition to central discretizations. Central schemes schemes do not consider any information about the wave propagation in the discretization, while upwind schemes determine the cell face fluxes according to the propagation direction. There are many flux functions available today to simulate the direction of the propagation of information in a flow field. According to Blazek and Toro they can be divided into two main groups as:[38, 3]

- Godunov Type Methods

- Flux Vector Splitting Methods

2.4 The Method of Godunov

Godunov type methods are first group of upwind methods. They use the piecewise (cell-averaged or slope limited) data in each cell to construct the left and right states at every mesh face. Then, interface fluxes are computed by solving the Riemann Problem, exactly or approximately, on that interface. Therefore, local properties of basic solutions to the Euler equations are directly introduced in the discretization strategy. The method is originally proposed by Godunov with first-order, cell averaged data reconstruction and exact Riemann-based flux function.

2.4.1 Riemann Problem

The Riemann problem is an initial value problem(IVP) with a discontinuous initial profile for hyperbolic systems. The initial profile is constant two different states at both sides of a discontinuity at $x = 0$. The Riemann problem for the one dimensional Euler equations can be written as given below

$$\frac{\partial \overrightarrow{Q}}{\partial t} + \frac{\partial \overrightarrow{F}(\overrightarrow{Q})}{\partial x} = 0 \tag{2.19}$$

$$\overrightarrow{Q} = \begin{bmatrix} \rho \\ \rho u \\ E \end{bmatrix}, \overrightarrow{F} = \begin{bmatrix} \rho u \\ \rho u^2 + p \\ u(E+p) \end{bmatrix} \tag{2.20}$$

with initial conditions stated as

$$\overrightarrow{Q}(x, t_0) = \begin{cases} \overrightarrow{Q}_L & if x < 0 \\ \overrightarrow{Q}_R & if x > 0 \end{cases} \tag{2.21}$$

In case of Euler equations, Riemann problem is is an extended shock tube problem. The shock tube problem consists of two stationary gases in a tube that are separated by a diaphragm. Then the diapghram ruptures and a wave structure builds up.

If the viscous effects are neglected and an infinitely long tube is taken into consideration, the flow following the rupture of the diaphragm can be obtained by the exact solution of the Euler equations. The solution combines shock waves, contact discontinuity, and rarefaction waves. In the Riemann problem, left and right particle speeds, u_L and u_R, can be non–zero, but the solution procedure of the problem is the same as the shock–tube problem.

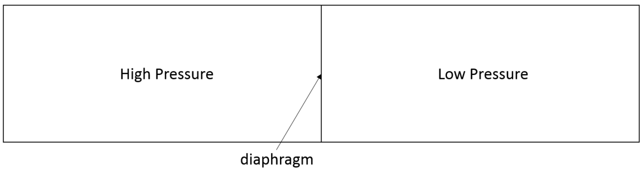

Figure 2.2: Sod's shock tube problem.

Solution of the Riemann problem is constant along the lines x/t. Therefore, the Riemann problem has four constant states, which are separated by the three waves corresponding to the three eigenvalues with speeds u,$u \pm a$. The middle wave is always a contact discontinuity, while the left and right waves can be either shock or expansion waves. Each wave separates two constant states on the left and right side of the wave. The wedge between the two non-linear waves is called the star region and is separated by the contact discontinuity in the two constant states $\overrightarrow{Q}_{*L}$,$\overrightarrow{Q}_{*R}$, which are the states respectively on the left and right side of the contact discontinuity. The velocity, u^*, and the pressure, p^*, in the star region are constant where densities take two different values ρ_L^*, ρ_R^*. From left to right solution has the four constant states $\overrightarrow{Q}_L$,$\overrightarrow{Q}_{*L}$,$\overrightarrow{Q}_{*R}$,$\overrightarrow{Q}_R$.

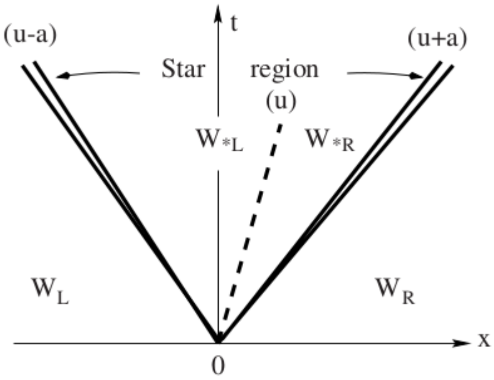

Figure 2.3: Structure of the Riemann problem solution for Euler equations.[3]

According to the generated wave type, there can be four different wave patterns. A complete solution of the Riemann problem requires the determination of the types of the waves, their relative strenghts, and the flow properties in each region between the waves and the contact surface.

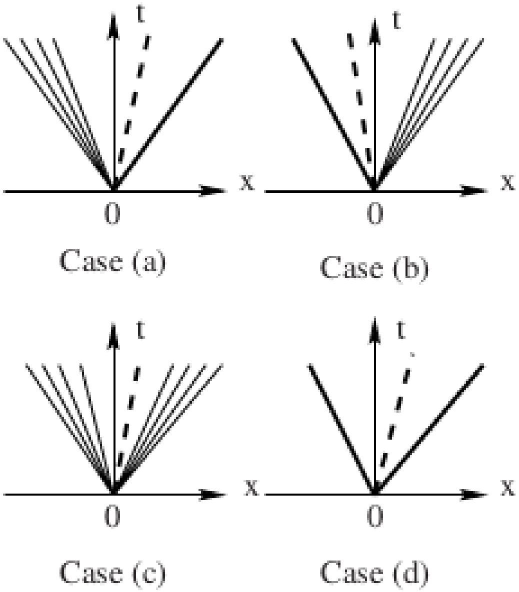

Figure 2.4: Possible wave patterns of the Riemann problem solution for Euler equations.[3]

Riemann problem has a similarity solution $\overrightarrow{Q}(x/t)$, and depends on the ratio of space and time coordinates x/t and the data states $\overrightarrow{Q}_L$, $\overrightarrow{Q}_R$.

2.4.2 Godunov Approach

Godunov has suggested a finite volume method[16] in 1959 to solve fluid dynamics problems with a large number of shock waves and contact discontinuities. In his method, solution is considered as piecewise constant over each volume at a fixed time $t = t^n$[4].

This generates local Riemann problems, which are centered at the boundaries between adjacent cells. The cell interfaces seperate two different fluid states $\overrightarrow{Q}_L$ at the left side and $\overrightarrow{Q}_R$ at the right side, like the diaphragm in the shock tube.

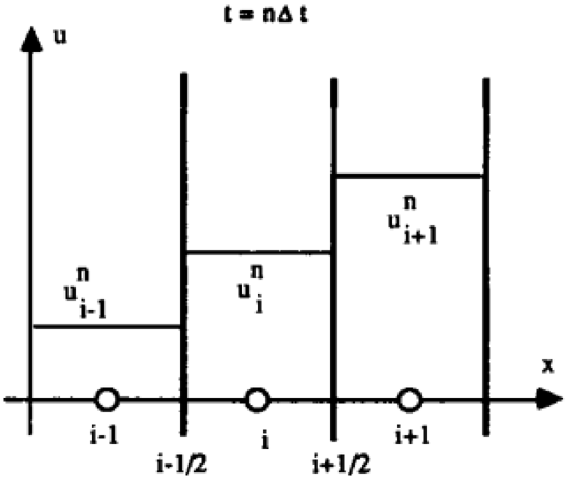

Figure 2.5: Piecewise constant distribution.[4]

Godunov recommended advancing the solution to a next time step $t = t^{n+1}$ by numerical fluxes, which are evaluated by the solution of local Riemann problems for Euler equations at cell interfaces. For one dimensional problems the Godunov scheme is written as

$$\overrightarrow{Q}^{n+1} = \overrightarrow{Q}^{n} + \frac{\Delta t}{\Delta x}(\overrightarrow{F}_{i-\frac{1}{2}} - \overrightarrow{F}_{i+\frac{1}{2}}) \tag{2.22}$$

with intercell numerical flux given by

$$\overrightarrow{F}_{i+\frac{1}{2}} = \overrightarrow{R}(\overrightarrow{Q}_L, \overrightarrow{Q}_R) \tag{2.23}$$

where $\overrightarrow{Q}_{i+\frac{1}{2}}(0)$ is the solution of the Riemann Problem$(\overrightarrow{Q}_L, \overrightarrow{Q}_R)$ along the ray $x/t = 0$. For original first-order method right and left states are assumed to be equal to the cell average. Godunov assumes that no wave interaction takes place within each cell. Therefore, to use this methodology, Δt , should be limited by the condition that the adjacent Riemann problems do not interfere.

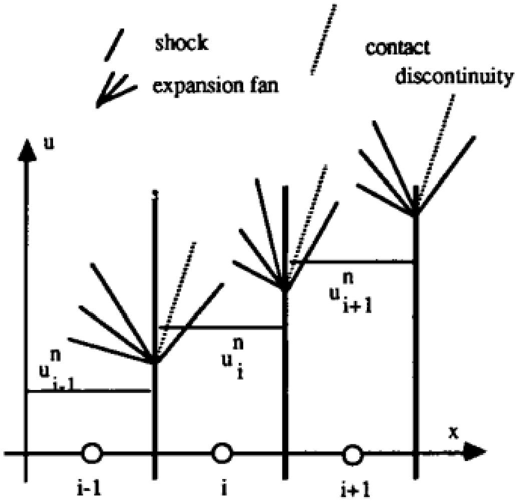

Figure 2.6: Reimann problem solution at interaces.[4]

2.4.3 Exact Solution of Riemann Problem

Most important part of the Godunov's method is the solution of the Riemann problem. An analytic solution of the Riemann problem for the Euler equations is unavailable, not even for ideal gases. However, it is possible to compute the solution numerically by iterative methods to any degree of accuracy. In order to obtain the complete solution solution at the contact discontinuity should be evaluated with an iterative process. This region is cshown in Figure 2.3, and called the star region. After the flow properties(p^*, u^*, ρ_L^*, ρ_R^*) are evaluated, all wave can be calculated.

The exact solution procedure, which is based on Rankine-Huoniot conditions, exploits the constancy of the velocity and pressure values in star region. The solution for pressure p^* and the u^* of the Riemann problem for Euler equations obeying the caloric EoS

$$e = \frac{p}{\rho(\gamma - 1)} \tag{2.24}$$

is given by following non-linear, algebraic equations

$$f_L(p) + f_R(p) + (u_R - u_L) = 0 \tag{2.25}$$

where

$$f_L(p) = \begin{cases} (p - p_L)\sqrt{\frac{2}{\rho_L(p(\gamma+1)+p_L(\gamma-1))}} & ifp > p_L(shock) \\ \frac{2a_L}{\gamma-1}\left(\left(\frac{p}{p_L}\right)^{\frac{\gamma-1}{2\gamma}} - 1\right) & ifp \leq p_L(rarefaction) \end{cases} \tag{2.26}$$

$$f_R(p) = \begin{cases} (p - p_R)\sqrt{\frac{2}{\rho_R(p(\gamma+1)+p_R(\gamma-1))}} & ifp > p_R(shock) \\ \frac{2a_R}{\gamma-1}\left(\left(\frac{p}{p_R}\right)^{\frac{\gamma-1}{2\gamma}} - 1\right) & ifp \leq p_L(rarefaction) \end{cases} \tag{2.27}$$

These equations may be solved iteratively to obtain p^* with Newton- Raphson method. This method requires and very dependent on inital start value ,p_0, to find the root in less iteration. More detailed information about method and the effect of the initial guess can be found in Toro's book [3] chapter 4. Once p^* is obtained u^* value can be obtained from

$$u^* = \frac{1}{2}(u_R + u_L) + \frac{1}{2}[f_R(p^*) - f_L(p^*)] \tag{2.28}$$

and ρ^*_R, ρ^*_L from isentropic relations. The solution of Riemann problem for x-split three-dimensional Euler equations is basically the same as the solution for corresponding one-dimensional problem for the quantities p, u, ρ.

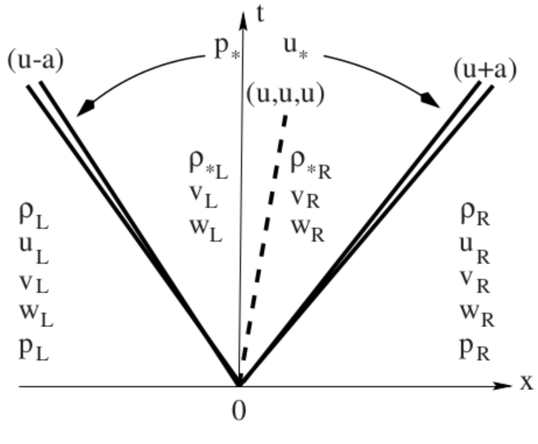

Figure 2.7: Structure of the Riemann problem solution for the three-dimensional case.[3]

There are two additional characteristic fields related with the two eigenvalues at speed u. These shear waves are related with the tangential velocity components w and v. These components are obtained with upwind manner as

$$q(x,t) = \begin{cases} q_R & if \frac{x}{t} < u^* \\ q_L & if \frac{x}{t} > u^* \end{cases} \tag{2.29}$$

where q represents v and w.

2.4.4 Approximate Riemann Solvers

Exact Riemann solvers can calculate the solution of the Riemann problem for Euler equations (2.17) by an iterative method. It is a computationally expensive procedure. In order to avoid this iterative method, approximate Riemann solvers are commonly employed for estimation of numerical fluxes. These solvers are preferred due to their simplicity and acceptable accuracy. Some traditional examples of approximate Riemann solvers are given below.

2.4.4.1 Roe Flux

The most popular of all approximate Riemann solvers is Roe's approximate solver, which was first presented in 1981[21]. To avoid the computationally expensive iterative operations of the Riemann problem, Roe linearized the Euler equations about an average state and then solved exactly by splitting the flux difference between two computational cells into contributions from forward-moving and backward-moving waves according to the direction of wave propagation. Among various approximate flux functions, the Roe scheme is well known for its accuracy. The three-dimensional numerical flux across the cell interface is written as

$$\overrightarrow{F}_{ROE} = \frac{F_L + F_R}{2} - \frac{\hat{A}\Delta\overrightarrow{Q}}{2} \tag{2.30}$$

where $\Delta Q = Q_R - Q_L$ and $\hat{A}$ is the x-direction Jacobian matrix of Euler equatipons, which constructed with Roe-averaged quantities.

$$\hat{A} = \begin{bmatrix} 0 & 1 & 0 & 0 & 0 \\ (\gamma-1)\hat{H}-\hat{u}^2-\hat{a}^2 & (3-\gamma)\hat{u} & -(\gamma-1)\hat{v} & -(\gamma-1)\hat{w} & (\gamma-1) \\ -\hat{u}\hat{v} & \hat{v} & \hat{u} & 0 & 0 \\ -\hat{u}\hat{w} & \hat{w} & 0 & \hat{u} & 0 \\ \frac{1}{2}\hat{u}[(\gamma-3)\hat{H}-\hat{a}^2] & \hat{H}-(\gamma-1)\hat{u}^2 & -(\gamma-1)\hat{u}\hat{v} & -(\gamma-1)\hat{u}\hat{w} & \gamma\hat{u} \end{bmatrix} \tag{2.31}$$

These quatities, denoted by hats, are averaged by weighting with $\sqrt{\rho}$ as following

$$\hat{\rho} = \sqrt{\rho_L \rho_R} \tag{2.32}$$

$$\hat{u} = \frac{u_L\sqrt{\rho_L} + u_R\sqrt{\rho_R}}{\sqrt{\rho_L} + \sqrt{\rho_R}} \tag{2.33}$$

$$\hat{v} = \frac{v_L\sqrt{\rho_L} + v_R\sqrt{\rho_R}}{\sqrt{\rho_L} + \sqrt{\rho_R}} \tag{2.34}$$

$$\hat{w} = \frac{w_L\sqrt{\rho_L} + w_R\sqrt{\rho_R}}{\sqrt{\rho_L} + \sqrt{\rho_R}} \tag{2.35}$$

$$\hat{H} = \frac{H_L\sqrt{\rho_L} + H_R\sqrt{\rho_R}}{\sqrt{\rho_L} + \sqrt{\rho_R}} \tag{2.36}$$

$$\hat{a} = \sqrt{(\gamma-1)(\hat{H} - \frac{(\hat{u}^2+\hat{v}^2+\hat{w}^2)}{2})} \tag{2.37}$$

The term $\hat{A}\Delta Q$ can be rewritten in the following form

$$\hat{A}\Delta\overrightarrow{Q} = \sum_{i=1}^{5} \hat{\alpha}_i \left|\hat{\lambda}_i\right| \hat{R}_i \tag{2.38}$$

where $\hat{\alpha}_i$ stands for wave strengths,$\hat{\lambda}_i$ for eigenvalues and $\hat{R}_i$ for right eigenvectors of the Jacobian matrix $\hat{A}$. Detailed information on methodologies to find $\hat{\alpha}_i$,$\hat{\lambda}_i$ and $\hat{R}_i$ readers is referred to Toro [3] chapter 11.

2.4.4.2 HLLC Flux

An approach is introduced by Harten Lax and van Leer [19] in 1983 to solving the Riemann problem approximately. The main idea in the solver is the assumption of a wave configuration which consists of two waves instead of three. The resulting solver forms the basis of a family of very accurate and robust Godunov type methods.

Main shortcoming of the original method is ignoring the presence of intermediate waves. Because of that, the resolution of physical features such as contact discontinuity and shear waves could be very inaccurate. A more accurate method, HLLC [22], proposed by Toro in 1992. This HLLC accepts three–wave solution of the Riemann problem with a more satisfactory resolution of middle waves. This method assumes a middle zone, including a contact discontinuity, divided by the right and left going waves.

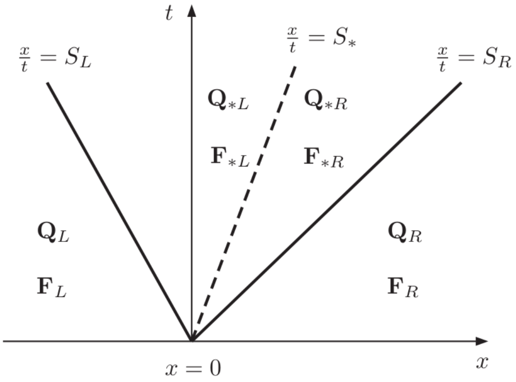

Figure 2.8: Wave model for the HLLC solver.[5]

The three-dimensional flux term for the interface with normal in the x-direction was given by Toro as follows

$$\overrightarrow{F}_{HLLC} = \begin{cases} \overrightarrow{F}_L & if S_L \geq 0 \\ \overrightarrow{F}_{*L} = \overrightarrow{F}_L + S_L(\overrightarrow{Q}_{*L} - \overrightarrow{Q}_L) & if S_L < 0 \cap S_* \geq 0 \\ \overrightarrow{F}_{*R} = \overrightarrow{F}_R + S_R(\overrightarrow{Q}_{*R} - \overrightarrow{Q}_R) & if S_R > 0 \cap S_* \leq 0 \\ \overrightarrow{F}_R & if S_R \leq 0 \end{cases} \tag{2.39}$$

Where two intermediate states in the star region $\overrightarrow{Q_{*L}}$ and $\overrightarrow{Q_{*R}}$,which are seperated by the contact discontiunity, were determined from equation (2.40).

$$\overrightarrow{Q_{*L/R}} = \frac{S_{L/R} - u_{L/R}}{S_{L/R} - S_*} \begin{bmatrix} \rho_{L/R} \\ \rho_{L/R} S_* \\ \rho_{L/R} v_{L/R} \\ \rho_{L/R} w_{L/R} \\ E_{L/R} + (S_* - u_{L/R})(\rho_{L/R} S_* + \frac{\rho_{L/R}}{S_{L/R} - u_{L/R}} \end{bmatrix} \tag{2.40}$$

The middle wave speed S_* can be calculated by the expression (2.41).

$$S_* = \frac{p_R - p_L + \rho_L u_L (S_L - u_L) - \rho_R u_R (S_R - u_R)}{\rho_L (S_L - u_L) - \rho_R (S_R - u_R)} \tag{2.41}$$

The left and right wave speed estimation method based on Roe averaged values is proposed by Einfeldt [20].

$$S_L = min(u_L - a_L, \hat{u} - \hat{c}), S_R = max(u_L - a_L, \hat{u} - \hat{c}) \tag{2.42}$$

$$\hat{u} = \frac{u_L \sqrt{\rho_L} + u_R \sqrt{\rho_R}}{\sqrt{\rho_L} + \sqrt{\rho_R}} \tag{2.43}$$

$$\hat{c}^2 = \frac{c_L^2 \sqrt{\rho_L} + c_R^2 \sqrt{\rho_R}}{\sqrt{\rho_L} + \sqrt{\rho_R}} + \frac{\sqrt{\rho_L}\sqrt{\rho_R}}{2(\sqrt{\rho_L} + \sqrt{\rho_R})^2} (u_R - u_L)^2 \tag{2.44}$$

With simple and accurate formulation, the HLLC is one of the most popular and adjustable approximate solvers in the literature. For years, the HLLC solver has been applied to various CFD applications.

2.5 Flux Vector Splitting Methods

The Flux Vector Splitting (FVS) Methods are considered as the more general definition of upwind schemes. They only account for the sign of the eigenvalues of the Euler equations to compute numerical flux at cell interface. The flux vector F at the cell center is simply split into components stemmed from the waves traveling to upstream and downstream directions, F^+ and F^-. Then, intercell numerical flux $F_{i+1/2}$

is constructed from two contributions; one comes from the forward component F_i^+ in the left cell and the other comes from the backward component F_{i+1}^- of right cell as shown in2.9.

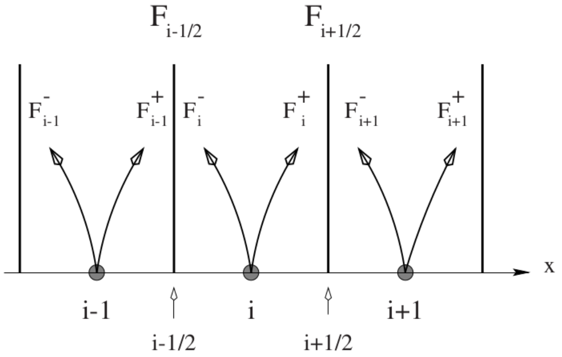

Figure 2.9: Splitting of the flux for cell i.[3]

FVS approach comes from homogenity property of hyperpolic type system of equations. Time dependent Euler equations 2.17 satisfy this requirement as follows

$$\overrightarrow{F} = \hat{A}\overrightarrow{Q} \tag{2.45}$$

Where $\hat{A}$ is the jacobian matrix 2.31 of Euler eqautions. Therefore, flux term can be constructed by splitting $\hat{A}$ into two component $\hat{A}^+$ and $\hat{A}^-$ under the restriction of its negatif and positive eigenvalues as follows

$$\overrightarrow{F_{i+1/2}} = \overrightarrow{F_i^+} + \overrightarrow{F_{i+1}^-} \tag{2.46}$$

$$\overrightarrow{F_i^+} = \hat{A}_i^+\overrightarrow{Q_i}, \qquad \overrightarrow{F_{i+1}^-} = \hat{A}_{i+1}^-\overrightarrow{Q_{i+1}} \tag{2.47}$$

FVS methods are computationally less expensive than Godunov type Riemann solvers. However, they have excessive numerical dissipation because of the lack of the entropy wave. The well-known FVS schemes presented by Steger- Warming [17], and Van Leer [18] are more efficient but considerably less accurate than Roe's solver.

The promiment family of FVS solvers in today's are AUSM based solvers. These solvers are superior to the classical FVS methods due to their superior shock-capturing features. These solvers and their implementations will be explained in detail in the next chapter.

CHAPTER 3

SHOCK-CAPTURING METHODS

The aforementioned traditional solvers have robust and accurate characteristics for many flow applications. However, they are inadequate for high-speed, viscous flow solutions. In this research, AUSM-family schemes and artificial-viscosity based methods are explored and implemented into the in-house compressible flow solver to resolve this problem. This chapter describes the detailed methodology and constructions of these methods.

3.1 AUSM-family Schemes

The Advection Upstream Splitting Method (AUSM) is a flux splitting method introduced by Liou and Steffen in 1991 [29]. Developers of the method aimed to design a new algorithm that is as efficient as flux vector splitting schemes and as accurate as the Godunov type schemes for high-speed flow calculations. The method has been formulated on the Euler equations. The key idea is to split inviscid flux into the two physically distinct parts, namely convective and pressure fluxes, and discretize them separately. The convective terms were considered as passive scalar quantities convected by interface velocity. On the other hand, pressure terms were governed by acoustic waves. Also, by its simple discretization strategy, AUSM is easliy extendable to fluid calculations other than the ideal gas. This is a critical feature for hypersonic flow simulations. The three-dimensional flux term for the interface with normal in the x-direction is written as follows

$$\overrightarrow{F} = \begin{bmatrix} \rho u \\ \rho u^2 + p \\ \rho uv \\ \rho uw \\ \rho uH \end{bmatrix} = \overrightarrow{F^{(c)}} + \overrightarrow{F^{(p)}} = u \begin{bmatrix} \rho \\ \rho u \\ \rho v \\ \rho w \\ \rho H \end{bmatrix} + \begin{bmatrix} 0 \\ p \\ 0 \\ 0 \\ 0 \end{bmatrix} \tag{3.1}$$

where H is the enthalpy per unit mass, defined by

$$H = \frac{E + P}{\rho} \tag{3.2}$$

In order to define intercell numerical flux $\overrightarrow{F_{1/2}}$ in terms of right and left states, Liou and Steffen took

$$\overrightarrow{F_{1/2}} = \overrightarrow{F^{(c)}_{1/2}} + \overrightarrow{F^{(p)}_{1/2}} \tag{3.3}$$

and defined convective flux $\overrightarrow{F^{(c)}_{1/2}}$, by introducing advective velocity $u_{1/2} = M_{1/2} a_{L/R}$, as

$$\overrightarrow{F^{(c)}_{1/2}} = u_{1/2} \begin{bmatrix} \rho \\ \rho u \\ \rho v \\ \rho w \\ \rho H \end{bmatrix}_{L/R} = M_{1/2} \begin{bmatrix} \rho a \\ \rho a u \\ \rho a v \\ \rho a w \\ \rho a H \end{bmatrix}_{L/R} \tag{3.4}$$

with definition

$$[*]_{L/R} = \begin{cases} [*]_L & if M_{1/2} \geq 0 \\ [*]_R & if M_{1/2} \leq 0 \end{cases} \tag{3.5}$$

Advection Mach number $M_{1/2}$ was given as a sum of the contributions of left and right states split Mach numbers

$$M_{L/R} = \frac{u_{L/R}}{a_{L/R}} \tag{3.6}$$

$$M_{1/2} = M_L^+ + M_R^- \tag{3.7}$$

by splitting just as in the Van Leer's flux vector splitting relations

$$M^{\pm} = \begin{cases} \pm\frac{1}{4}(M \pm 1)^2, & if\,|M| \le 1 \\ \frac{1}{2}(M \pm |M|), & if\,|M| > 1 \end{cases} \tag{3.8}$$

For calculating presssure flux $\overrightarrow{F^{(p)}_{1/2}}$, pressure term $p_{1/2}$ was given as

$$p_{1/2} = p^{+}_{L}.p_{L}. + p^{-}_{R}.p_{R} \tag{3.9}$$

which was split by using polynomial expansions of the characteristic speeds

$$p^{\pm} = \begin{cases} \frac{1}{4}(M \pm 1)^2(2 \mp M), & if\,|M| \le 1 \\ \frac{1}{2}\frac{(M \pm |M|)}{M}, & if\,|M| > 1 \end{cases} \tag{3.10}$$

Finally flux term was expressed as

$$\overrightarrow{F}_{AUSM} = \frac{M_{1/2} + \left|M_{1/2}\right|}{2} \begin{bmatrix} \rho a \\ \rho a u \\ \rho a v \\ \rho a w \\ \rho a H \end{bmatrix}_L + \frac{M_{1/2} - \left|M_{1/2}\right|}{2} \begin{bmatrix} \rho a \\ \rho a u \\ \rho a v \\ \rho a w \\ \rho a H \end{bmatrix}_R + \begin{bmatrix} 0 \\ p_{1/2} \\ 0 \\ 0 \\ 0 \end{bmatrix} \tag{3.11}$$

Splitting the inviscid flux into its convective and pressure components opens up a new family of inviscid flux functions. Many improvements were proposed as the "AUSM-family" schemes upon the formulation chosen for convective and pressure fluxes. Structures and methodologies of prominent AUSM-family schemes 3.1, which preserve the solution robustness and accuracy in high-speed visocus flow simulations, are given below.

3.1.1 AUSM+up

The first improved version of the original AUSM, AUSM+[42], was introduced by one of the original authors of AUSM, Liou. The new version of the scheme has several desirable features:

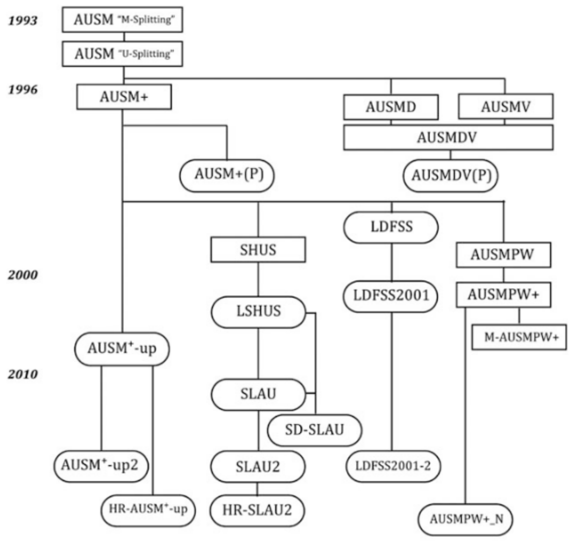

Figure 3.1: AUSM (Advection Upstream Splitting Method) family tree.[6]

- high resolution of contact discontinuities and normal stationary shocks
- preserving positivity of scalar quantities
- free of oscillations and anomalies at stationary and moving shocks.

More advanced Mach number and pressure term splittings were introduced in the new formulation for better accuracy. Also, Mach number and velocity splittings were unified by introducing a common speed of sound term $a_{1/2}$ at interface.

$$u_{1/2} = M_{1/2} a_{1/2} \tag{3.12}$$

Despite success in high speed external fow simulations practice, AUSM+ revealed that it could not preserve its robustness and accuracy in low-speed regions. To overcome this issue, Liou introduced AUSM+up [30], an extension of AUSM+, for flows at all-speed regimes. Inserting additional velocity M_p and pressure diffusion p_u to the flux resulted in a more stable and accurate scheme. The x-split formulation of algorithm is given as follows

$$M_{L/R} = \frac{u_{L/R}}{a_{1/2}} \tag{3.13}$$

$$M_{1/2} = M_L^+ + M_R^- + M_p \tag{3.14}$$

$$M^{\pm} = \begin{cases} \pm\frac{1}{4}(M \pm 1)^2 \pm \beta(M^2 - 1)^2, & if\,|M| \leq 1 \\ \frac{1}{2}(M \pm |M|), & if\,|M| > 1 \end{cases} \tag{3.15}$$

$$M_p = -\frac{K_P}{f_a} max((1 - \sigma\bar{M}^2), 0)\frac{p_R - p_L}{\bar{\rho} a_{1/2}^2} \tag{3.16}$$

$$p_{1/2} = p_L^+ . p_L . + p_R^- . p_R + p_u \tag{3.17}$$

$$p^{\pm} = \begin{cases} \frac{1}{4}(M \pm 1)^2(2 \mp M) \pm \alpha M(M^2 - 1)^2, & if\,|M| \leq 1 \\ \frac{1}{2}\frac{(M \pm |M|)}{M}, & if\,|M| > 1 \end{cases} \tag{3.18}$$

$$p_u = -K_u p_L^+ p_R^- (\rho_L + \rho_R)(f_a a_{1/2})(u_R - u_L) \tag{3.19}$$

The common speed of sound incorporates the information of flow direction into flux evaluation,which supress generation of unnecessary expansion shocks. Formulation of it was given by Liou as

$$a_{1/2} = min(\tilde{a_L}, \tilde{a_R}) \tag{3.20}$$

where

$$\tilde{a_L} = \frac{(a^*)^2}{max(a^*, u_L)}, \tilde{a_R} = \frac{(a^*)^2}{max(a^*, -u_R)} \tag{3.21}$$

The critical speed of sound a^* formulation was given as

$$(a^*)^2 = \frac{2(\gamma - 1)}{\gamma + 1} H \tag{3.22}$$

Scaling function f_a was introduced to scale the numerical dissipation according to the flow speed.

$$f_a = M_o(2 - M_o) \tag{3.23}$$

Recommended values and formulations of necessary parameters for all-speed extension of the algorithm were given as

$$\beta = \frac{1}{8}, K_p = 0.25, K_u = 0.75, \sigma = 1 \tag{3.24}$$

$$\bar{\rho} = \frac{\rho_L + \rho_R}{2} \tag{3.25}$$

$$\bar{M}^2 = \frac{u_L^2 + u_R^2}{2a_{1/2}^2} \tag{3.26}$$

$$(M_o)^2 = min(1, max(\bar{M}^2, M_{co}^2)) \tag{3.27}$$

$$\alpha = \frac{3}{16}(-4 + 5f_a^2) \tag{3.28}$$

The cutoff Mach number, M_{co}, is a user-defined parameter, inherited from the preconditioning procedures. Especially for external flow solutions, it is chosen as the free-stream Mach number.

$$M_{co} = M_\infty \tag{3.29}$$

The final form of numerical flux is defined as

$$\vec{F}_{AUSM+up} = \frac{M_{1/2}a_{1/2} + |M_{1/2}a_{1/2}|}{2} \begin{bmatrix} \rho \\ \rho u \\ \rho v \\ \rho w \\ \rho H \end{bmatrix}_L + \frac{M_{1/2}a_{1/2} - |M_{1/2}a_{1/2}|}{2} \begin{bmatrix} \rho \\ \rho u \\ \rho v \\ \rho w \\ \rho H \end{bmatrix}_R + \begin{bmatrix} 0 \\ p_{1/2} \\ 0 \\ 0 \\ 0 \end{bmatrix}$$

3.1.2 SLAU and SLAU2

Existing all-speed flux schemes need at least one problem-dependent parameter, like cutoff Mach number in AUSM+-up, which can sometimes restrict the scheme's applicability. Simple Low-dissipation AUSM (SLAU) was introduced by Japanese scientists Kitamura and Shima in 2011 [31]. Developers aimed to create a new scheme without any tunable parameter while it keeps the robustness and accuracy of AUSM-family fluxes at all speed regimes. SLAU eliminated the need for the cutoff Mach number by scaling dissipative terms according to multidimensional velocities. The final form of the x-split flux with new mass flux and pressure term calculations is written as follows

$$\dot{m}_{1/2} = \frac{1}{2}(\rho_L(u_L + \left|\bar{V_n}\right|^+) + \rho_R(u_R - \left|\bar{V_n}\right|^-)) - \frac{\chi}{a_{1/2}}\triangle p \tag{3.30}$$

where

$$\left|\bar{V_n}\right|^+ = (1-g)\left|\bar{V_n}\right| + g\left|u_L\right|, \left|\bar{V_n}\right|^- = (1-g)\left|\bar{V_n}\right| + g\left|u_R\right| \tag{3.31}$$

$$\left|\bar{V_n}\right| = \frac{\rho_L\left|u_L\right| + \rho_R\left|u_R\right|}{\rho_L + \rho_R} \tag{3.32}$$

$$\triangle p = \left|p_L - p_R\right| \tag{3.33}$$

$$g = -max(min(M_L, 0), -1)min(max(M_R, 0), 1) \tag{3.34}$$

$$M_{L/R} = \frac{u_{L/R}}{a_{1/2}} \tag{3.35}$$

Definition of interface speed of sound $a_{1/2}$ was borrowed from AUSM+.

$$a_{1/2} = min(\tilde{a_L}, \tilde{a_R}) \tag{3.36}$$

$$\tilde{a} = \frac{(a^*)^2}{max(a^*, |u|)} \tag{3.37}$$

$$(a^*)^2 = \frac{2(\gamma-1)}{\gamma+1}H \tag{3.38}$$

$$\chi = (1-\hat{M})^2 \tag{3.39}$$

$$\hat{M} = min(1, \frac{1}{a_{1/2}}\sqrt{\frac{u_L^2 + v_L^2 + w_L^2 + u_R^2 + v_R^2 + w_R^2}{2}}) \tag{3.40}$$

New pressure term was introduced for calculation of pressure flux as

$$p_{1/2} = \frac{p_L + p_R}{2} + \frac{p_L^+ - p_R^-}{2}(p_L - p_R) + (1-\chi)(p_L^+ + p_R^- - 1)\frac{p_L + p_R}{2} \tag{3.41}$$

Pressure was split same as AUSM+up with $\alpha = 0$ for simplicty.

$$p^{\pm} = \begin{cases} \frac{1}{4}(M \pm 1)^2(2 \mp M), & if\,|M| \leq 1 \\ \frac{1}{2}\frac{(M \pm |M|)}{M}, & if\,|M| > 1 \end{cases} \tag{3.42}$$

Although its parameter-free nature differentiates SLAU from the other preceding AUSM-family flux functions, it still suffers from shock anomalies under certain conditions. Moreover, because the pressure term of SLAU is based on the ideal gas assumption, it is not extendable to real gas solutions. Therefore, to increase the robustness of SLAU against shock instabilities, developers proposed SLAU2. They discovered that numerical dissipation is limited to a constant value regardless of Mach number at supersonic flow speeds in the original scheme. And limited dissipation is insufficient for high supersonic Mach numbers. A new pressure term $p_{1/2}$ formulation was introduced to overcome this shortage. Also, with the new formulation of the pressure term, which is based on the perfect gas assumption, developers made SLAU2 free from that restriction. Modified pressure flux formulation was given as

$$p_{1/2} = \frac{p_L + p_R}{2} + \frac{p_L^+ - p_R^-}{2}(p_L - p_R) + \sqrt{\frac{u_L^2 + v_L^2 + w_L^2 + u_R^2 + v_R^2 + w_R^2}{2}}(p_L^+ + p_R^- - 1)\frac{\rho_L + \rho_R}{2}a_{1/2} \tag{3.43}$$

where

$$a_{1/2} = min(\tilde{a_L}, \tilde{a_R}) \tag{3.44}$$

$$\tilde{a} = \frac{(a^*)^2}{max(a^*, |u|)} \tag{3.45}$$

$$(a^*)^2 = \frac{2(\gamma - 1)}{\gamma + 1}H \tag{3.46}$$

$$p^{\pm} = \begin{cases} \frac{1}{4}(M \pm 1)^2(2 \mp M), & if\,|M| \leq 1 \\ \frac{1}{2}\frac{(M \pm |M|)}{M}, & if\,|M| > 1 \end{cases} \tag{3.47}$$

and the final form of SLAU2 is written as

$$\overrightarrow{F}_{SLAU2} = \frac{\dot{m}_{1/2} + \left|\dot{m}_{1/2}\right|}{2}\begin{bmatrix} 1 \\ u \\ v \\ w \\ H \end{bmatrix}_L + \frac{\dot{m}_{1/2} - \left|\dot{m}_{1/2}\right|}{2}\begin{bmatrix} 1 \\ u \\ v \\ w \\ H \end{bmatrix}_R + \begin{bmatrix} 0 \\ p_{1/2} \\ 0 \\ 0 \\ 0 \end{bmatrix} \tag{3.48}$$

3.2 Artifical Viscosity Methods for Curing Numerical Instabilities

In traditional shock-capturing methods, numerical dissipation provides the appropriate smearing of discontinuities, which is inherent in the schemes. Therefore, researchers generally explore the dissipative mechanisms of flux functions and try to control them to smooth out oscillations and anomalies near shock waves. In 1950, another methodology was introduced by Von Neumann and Richtmyer [14], which is based on the explicit introduction of numerical dissipation into the Euler equations to ensure the sufficient smearing of strong discontinuities. Since the introduced dissipative terms are in the form of physical viscosity, they are named artificial viscosity terms, and the methods based on this concept are called artificial viscosity methods. This additional dissipation is in the form of the right-hand side of the Navier-Stokes equations. In one-dimensional form, the artificial dissipation is given as in equation 3.49.

$$\frac{(c\Delta x)^2}{V}\frac{\partial u}{\partial x}\left|\frac{\partial u}{\partial x}\right| \tag{3.49}$$

where V and u are the specific volume and fluid velocity, respectively. c is a dimensionless constant near unity. This technique does not alter inviscid flux calculations, such that it can be combined with different inviscid flux schemes. This flexibilty of Artificial Viscosity methods is a very favorable feature. However, an appropriate method is required to ensure that the diffusion is applied to the shock layer only instead of the physically correct features present in the flowfield. Moreover, the artificial viscosity coefficient expression should cure the shock anomalies in a wide range of flow and geometry conditions without user-dependent parameters. To achieve these objectives, researchers try to generate sensors that maintain the accuracy of the general solution while applying the smallest amount of artificial viscosity to necessary regions.

3.2.1 Rodionov's Artificial Viscosity Method

In 2017, Russian researcher Alexander V. Rodionov proposed a new artificial viscosity approach to cure hypersonic flow instabilities [34]. He formulated a multidimensional artificial viscosity coherent with Von Neumann and Richtmyer's artificial viscosity 3.49 as given in equation 3.50.

$$\mu_{AV} = C_{AV}\rho h^2 \left|\nabla \cdot \overrightarrow{V}\right| \tag{3.50}$$

where C_{AV} is a dimensionless, user-dependent parameter and h is the characteristic mesh size. Because of the possibility of artificial viscosity dampening relevant information, it is vital to ensure that the artificial viscosity is applied only in areas where it is required. Therefore, Rodinov thresholded his approach only to compressed cells to achieve that goal as

$$\mu_{AV} = \begin{cases} C_{AV}\rho h^2 \left|\nabla \cdot \overrightarrow{V}\right| & if \nabla \cdot \overrightarrow{V} < 0 \\ 0 & otherwise \end{cases} \tag{3.51}$$

Then, to preserve the scheme quality in the shockless compression regions, he introduced a shock detection sensor, which based on characteristic mesh size and speed of sound a . The modified formulation was written as

$$\mu_{AV} = \begin{cases} C_{AV}\rho h^2 \sqrt{\left(\nabla \cdot \overrightarrow{V}\right)^2 - \left(C_{th}\frac{a}{h}\right)^2} & if \nabla \cdot \overrightarrow{V} < -C_{th}\frac{a}{h} \\ 0 & otherwise \end{cases} \tag{3.52}$$

where C_{th} is the threshold coefficient and it was chosen to be $C_{th} = 0.05$ as a result of numerous test simulations by Rodionov. Also, for more physically consistent solutions, he presented an artificial heat conductivity term as

$$k_{AV} = \frac{\mu_{AV} C_p}{Pr} \tag{3.53}$$

where C_p is the specific heat at constant pressure, Pr is the Prandtl number taken equal to 0.75. He presented an expression, which based on diagonal length of cells d_i for the characteristic mesh size in his formula as

$$h = \frac{max(d_i)}{\sqrt{3}}$$

and, calibrated C_{AV}^{min} according to that expression. However, calculating all of the diagonal lengths is a computationally expensive procedure. Therefore, in our work, characteristic mesh size derived as the cube root of cell volume $h = \sqrt[3]{V}$ for three dimensional solutions and root of cell area $h = \sqrt{A}$ for two dimensional ones. C_{AV}^{min} recalibration for this characteristic mesh size calculation will be presented in the next chapter. The resultant method is named Rodinov's artificial viscosity (RAV). By combining it with Roe and HLLC complete Reimann solvers, Roe+RAV and HLLC+RAV schemes are generated.

3.2.2 A Pressure Ratio Based Artificial Viscosity Method

Although, Rodionov demonstrated the efficiency of his method on several well-known test problems, his shock sensor structure is considered to be case-dependent because of dimensional parameters, cell size and speed of sound, in it. To avoid these dimensional parameters and to increase the application range of the method, a new pressure-ratio based shock sensor [7] is borrowed to detect shock waves and activate artificial viscosity. It's defined as

$$h_k = min\left(\frac{p_i}{p_k}, \frac{p_k}{p_i}\right) \tag{3.54}$$

$$h = \min_k(h_k) \tag{3.55}$$

$$g = \frac{1 + cos(\pi h)}{2} \tag{3.56}$$

The subscript k is the index for all neighboring interfaces of applied cells.

The function h selects the minimum value of h_k from all the adjacent interfaces as shown in Figure 3.2. Then, the function g embraces a strecth function to ensure a smoother transition of applied artificial viscosity. This sensor is applicable to both types of grids, structured and unstructured. In smooth regions, the function g tendsto zero because of the negligible change in the pressure value as given in Figure 3.3. In contrast, near discontinuities, the function g increases with the increase of pressure gradient.

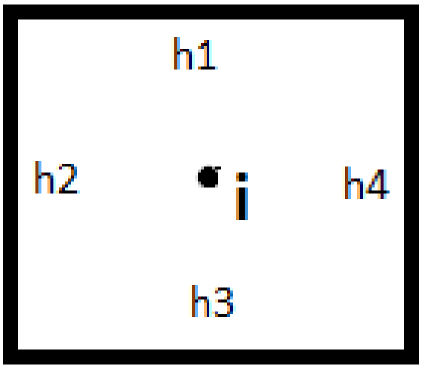

Figure 3.2: Illustration of the function h for cell i.

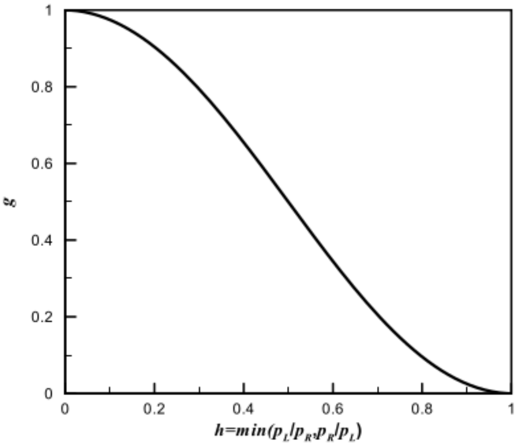

Figure 3.3: Pressure ratio based function g.[7]

Chen uses that term to scale his additional dissipation term, obtained from the difference between Roe and HLL flux functions. In this study, this term is used for scaling artificial viscosity as given in 3.57 . Self-generated sensor is named as pressure-ratio based artificial viscosity method(PRAV) and implemented to Rodionov's method as follows

$$\mu_{AV} = \begin{cases} gC_{AV}\rho h^2 \left|\nabla \cdot \overrightarrow{V}\right| & if \nabla \cdot \overrightarrow{V} < 0 \\ 0 & otherwise \end{cases} \tag{3.57}$$

Artificial heat conductivity term k_{AV} used in the same way as given in 3.53 without modification. That method is also combined with Roe and HLLC solvers and Roe+PRAV and HLLC+PRAV schemes are generated.

3.3 CFD Solver

All mentioned shock capturing methods are implemented in our finite volume solver. It is based on an open-source compressible flow solver, flowPsi, built on a rule-based programming framework, Loci.

Inviscid and viscous flux calculations in the solver are built as separate libraries. HLLC and Roe schemes are available in the inviscid flux library as standard C++ functions, which construct inviscid flux from the left and the right flow variables. Implemented AUSM-family schemes, AUSM+up and SLAU2, are designed and applied in a similar way to these schemes. On the other hand, the artificial viscosity term is formulated and implemented similarly to the molecular viscosity term in the viscous flux library.

All the runs are performed with implicit time stepping. A fast and robust sparse matrix solver, line-symmetric Gauss-Seidel, is used in these implicit computations. In analyses with second-order spatial accuracy, Green-Gauss reconstruction and the Venkatakrishnan limiter are used to form a sufficient condition, which avoids introducing oscillation in the solution process . Also, the $k-\omega$ SST model, which has high accuracy in external flow analysis, is used for simulations with turbulence modeling.

CHAPTER 4

NUMERICAL EXPERIMENTS AND RESULTS

This chapter presents several numerical tests to compare the implemented AUSM and artificial viscosity based shock-capturing schemes. The primary focus of this study is on investigating the accuracy and robustness of the implemented methods for viscous hypersonic problems.

Firstly, an inviscid hypersonic flow example is considered to show the capability of the proposed methods to solve problems with strong shocks. For this purpose, a well-known benchmark case is selected and used.

Then, a flat plate example follows this to understand the boundary-layer resolution capabilities of the implemeneted methods to ensure boundary layer simulations are unaffected due to inclusion of extra dissipation.

Finally in last test case, performances of the implemented methods are compared for calculations of three-dimensional simulations and heat transfer prediction. The problem solved here is the hypersonic flow past a ballistic rocket geometry (HB-2). With these validation cases, implemented methods are compared among each other and with the experimental data.

4.1 Hypersonic Inviscid Flow Over a Cylinder

Hypersonic inviscid flow past a cylinder is a typical problem [25, 8] for examining the catastrophic shock anomalies of low diffusion upwind schemes. As previously mentioned, shock-capturing methods, which have minimal dissipation, are generally vulnerable to shock instabilities such as the carbuncle phenomena.

4.1.1 Problem Set-Up

In this numerical experiment, a cylinder with a 0.5-meter radius is located in a uniform gas where the upstream Mach number is set as 20. The freestream conditions are selected to be the properties of air at sea level conditions, $T_\infty = 288.15\,\mathrm{K}$, $P_\infty = 101325\,\mathrm{Pa}$. All simulations are conducted with the first-order accurate spatial schemes with $CFL = 0.5$. All solutions are iterated up to 50000 steps unless shock anomalies cause a divergence.

Density contours computed by different schemes are illustrated to examine if instabilities occur. For that purpose, 30 contour levels varying from 2.0 to 8.5 are used. This severe test case is simulated to evaluate and compare the ability of implemented methods to capture strong shock waves.

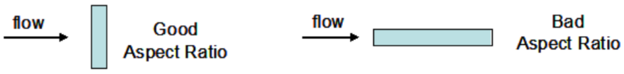

Figure 4.1: Aspect ratio of grids.[8]

Since shock instabilities are highly sensitive to computational mesh, generating a computational domain is the main task for systemically assessing the shock robustness of relevant methods. Henderson and Menart's [8] two main conclusions about mesh dependencies of shock instabilities are as follows:

- If the cell faces are more aligned with the shock wave, these faces introduce more numerical dissipation to the solution. Thus, the possibility of shock instabilities occurring is decreasing.
- Instabilities are independent of the computational cell size but mostly depend on the aspect ratio. A wide control volume parallel to the shock wave introduces numerical dissipation to the solution in that direction. Therefore, control volumes with short edges perpendicular to the shock wave and long edges parallel to it decrease the possibility of occurring shock instabilities, as given in the Figure 4.1.

According to these findings, a cylindrical shape computational domain is created as given in Figure 4.2.This domain type is designed to ensure that grid lines, dis-

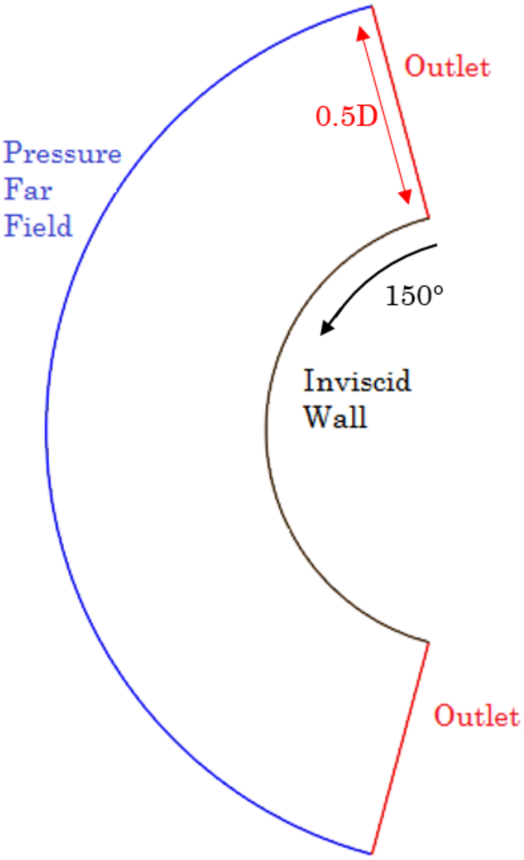

Figure 4.2: Solution domain with boundary conditions

tributed uniformly in both directions, around the bow shock wave do not align with it and shock instabilities are noticeable. The aspect ratio effect is investigated by changing the number of divisions in the radial direction while holding the number of mesh points in the circumferential direction constant as 321, which division is recommended in [2]. For this purpose, three different meshes with different radial division as given in Table 4.1 are generated and simulated with low-dissipative HLLC and Roe's schemes. Using meshes with lower aspect ratio cells would be impractical—that kind of meshes are only for special studies. So, they are not considered.

Density contours of solutions given in Figures 4.34.44.5 respectively. Results clearly show that even though the Roe scheme exhibits the aforementioned carbuncle anomaly, the HLLC scheme also produces incorrect density contours near the stagnation streamline. The reason, why the HLLC scheme does not produce as catastrophic as with the Roe flux, is that the solution of two-dimensional simulations of HLLC remains

Table 4.1: Uniform divisions of meshes with different aspect ratios.

Radial Division	Circumferential Division
90	321
125	321
250	321

bounded and can't produce disastrous oscillations as given in Reference [43].

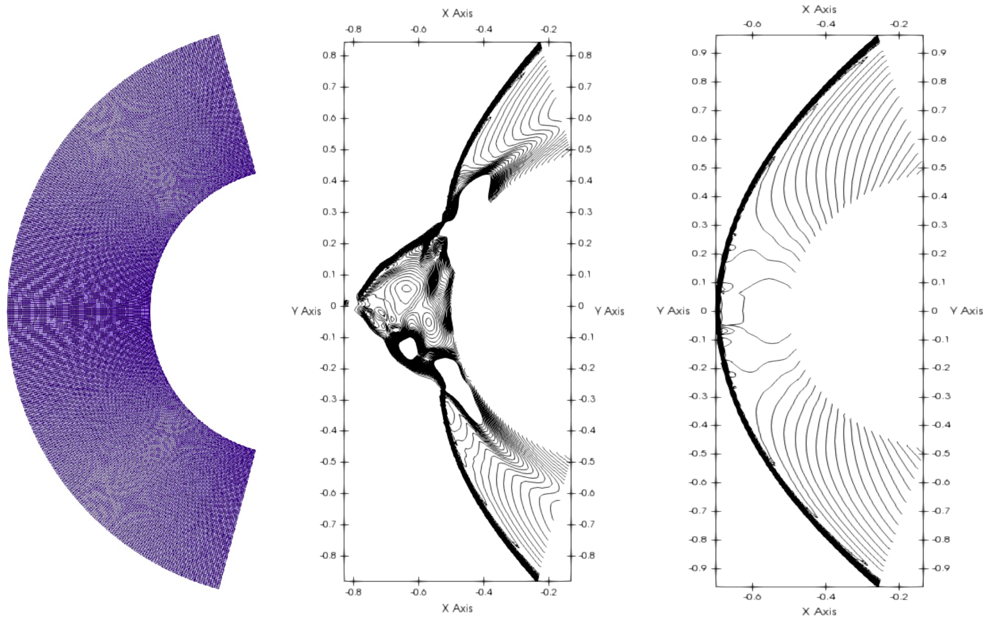

(a) Computational domain (b) Density contours of ROE flux (c) Density contours of HLLC flux

Figure 4.3: Computational domain and solutions of 90-321 grid

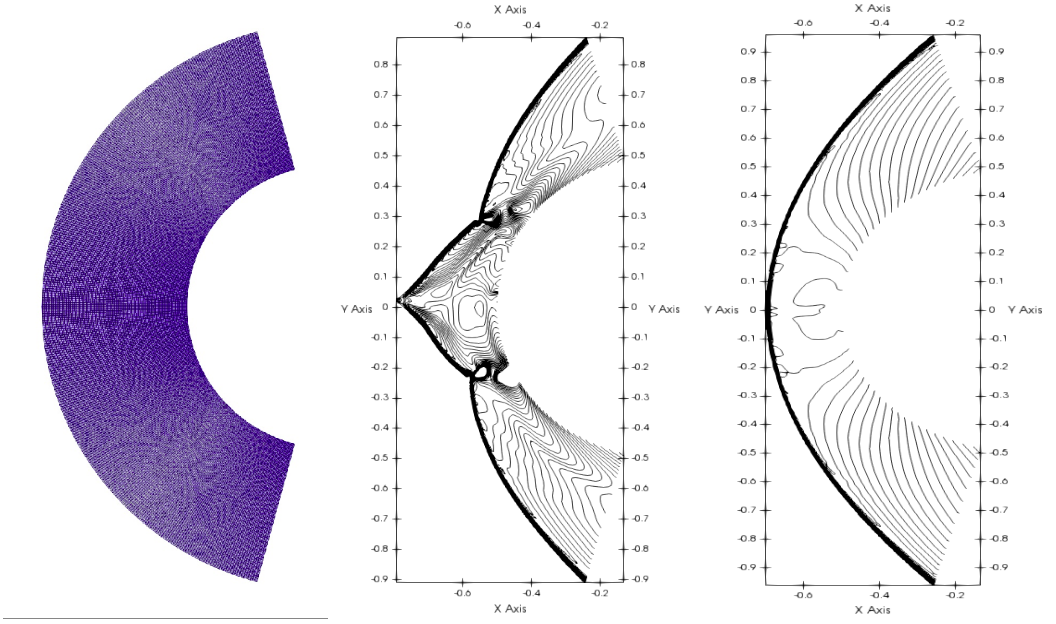

(a) Computational domain (b) Density contours of ROE flux (c) Density contours of HLLC flux

Figure 4.4: Computational domain and solutions of 125-321 grid

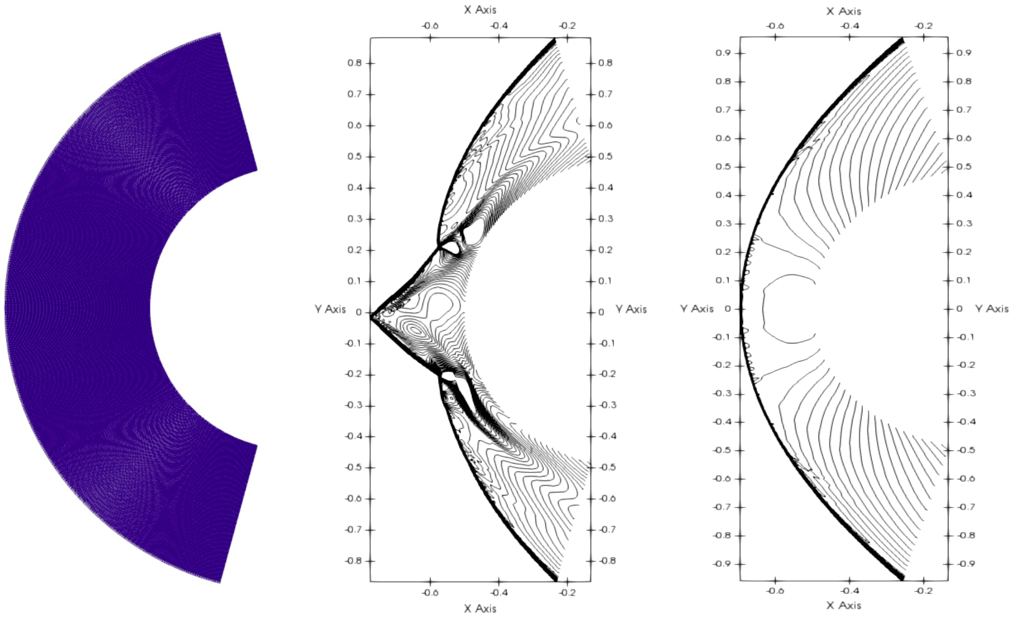

(a) Computational domain (b) Density contours of ROE flux (c) Density contours of HLLC flux

Figure 4.5: Computational domain and solutions of 250-321 grid

Shock instabilities are clearly observable for both schemes on the grid, with 125 grid points in the radial direction and 321 in the circumferential direction. Thus, this grid is used compare the shock-capturing capabilities of implemented methods.

This numerical experiment is used to calibrate the artificial viscosity based methods' C_{AV} parameters. This user-dependent parameters are calibrated to their minimum value to eliminate the relevant shock instabilities. Calibrated values, which are also used without changing in the following experiments, are presented in Table 4.2. Although our characteristic mesh size calculation methods are different, the minimum C_{AV} values of all artificial viscosity based schemes are found 0.3 as suggested by Rodinov.

Table 4.2: C_{AV} minimum calibrated values.

HLLC+PRAV	0.3
HLLC+RAV	0.3
ROE+PRAV	0.3
ROE+RAV	0.3

4.1.2 Results

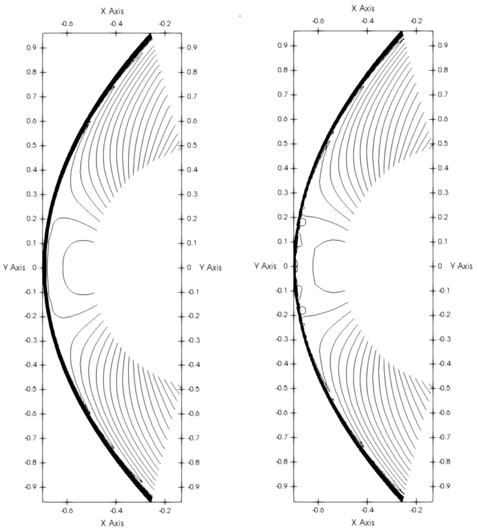

(a) SLAU scheme (b) AUSM+up scheme

Figure 4.6: Density contours of AUSM based methods

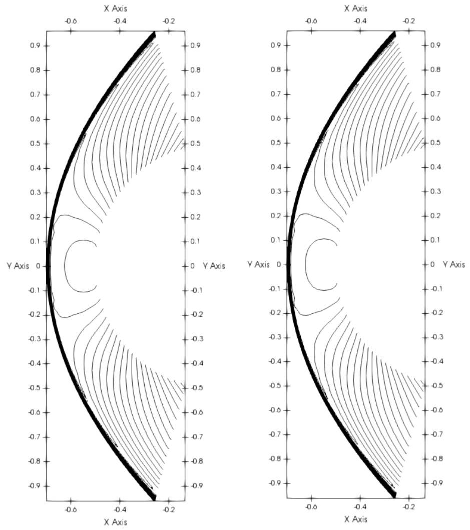

(a) ROE+RAV scheme (b) HLLC+RAV scheme

Figure 4.7: Density contours of RAV methods

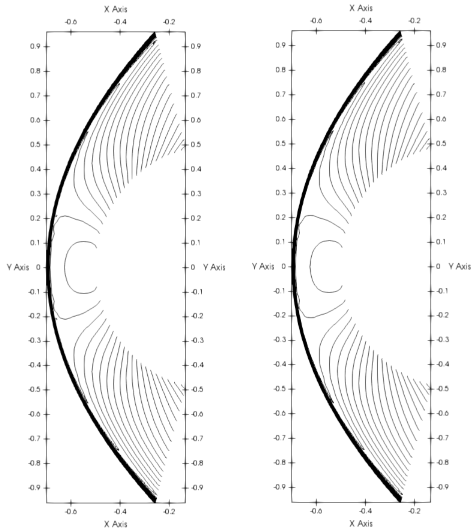

(a) ROE+PRAV scheme (b) HLLC+PRAV scheme

Figure 4.8: Density contours of PRAV methods

The computed results with implemented schemes are shown in Figures 4.64.74.8 . Also, density solutions of implemented methods over the stagnation line are presented in Figure 4.9 for detailed examination. The proposed SLAU2 scheme produced a clean shock profile, and its post-shock regions are free from shock anomalies. The AUSM+up scheme has a more wiggly solution in the shock region but is also free from shock anomalies. These solutions show that the presented all-speed AUSM schemes are highly resistant to strong shock waves.

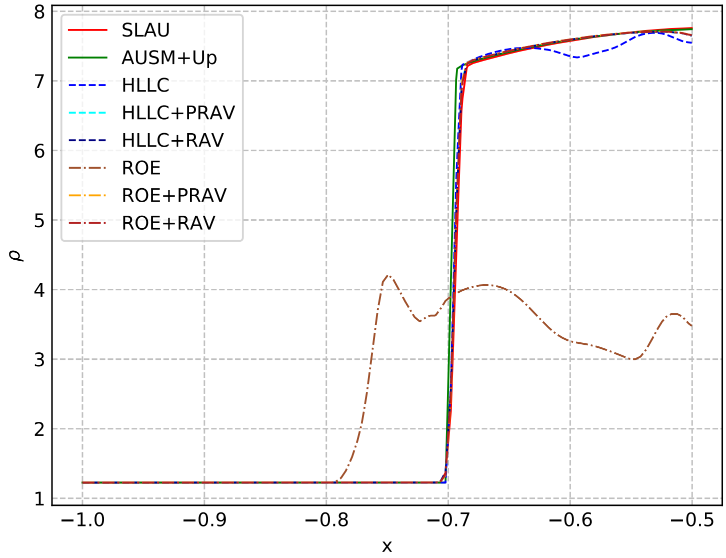

Figure 4.9: Densities over the stagnation line.

On the other hand, computational solutions for both artificial viscosity based methods are given, where nearly no visible shock instabilities and post-shock wiggles appear. High shock robustness is achieved by adding artificial viscosity to necessary regions. Compared with the corresponding original schemes' the results of those new schemes are greatly improved.

In Figure 4.10, contours of Mach number (top half) and artificial viscosity,μ_{AV}, (bottom half) computed by ROE+RAV and ROE+PRAV is presented. As can be seen, artificial viscosities in both schemes tend to their maximum near shock waves but zero in other regions. However, pressure-ratio based shock sensor still stands out with its advantages, such as not including case-dependent parameters like the speed of sound and mesh size.

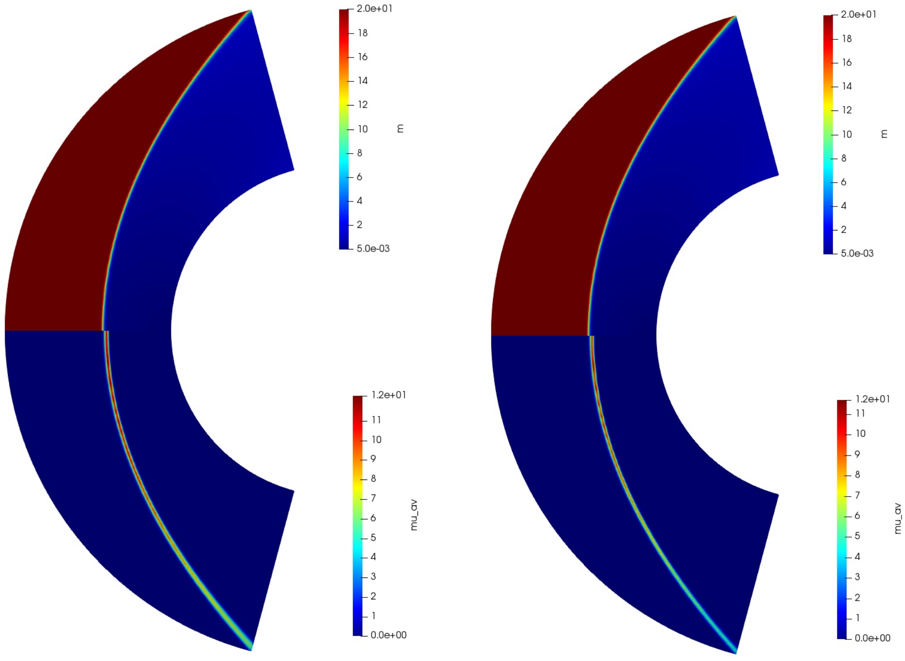

(a) ROE+RAV (b) ROE+PRAV

Figure 4.10: Contours of Mach number and artificial viscosity,μ_{AV}

By this numerical experiment, it has been ensured that the implemented schemes have high shock capture capabilities. The following two experiments will test whether this ability causes accuracy degradation throughout the resolving continuous gradients.

4.2 Subsonic Flat Plate

In the previous computational experiment, the shock-capturing abilities of the implemented methods were tested. This section is employed to ensure that the implemented methods do not affect the continuous gradients. For this aim, a subsonic flat plate problem is solved numerically in this section. The solution domain and boundary conditions are shown in Figure 4.11.

4.2.1 Problem Set-Up

The computational mesh4.12 is the 2nd most fine mesh out of five recommended to be used in flat plate validation studies by NASA[44]. The rectangular computational domain has 193 cells in the normal to wall direction and 273 cells in the streamwise direction. Grids are clustered toward the plate to keep the first cells $y+ \leq 1$ to resolve the viscous region accurately. Also, a dense mesh is defined at the leading edge of the flat plate to resolve the stagnation point with reasonable accuracy.

All solutions are calculated with second-order spatial accuracy. The computations are conducted for 20000 steps and CFL numbers are increased up to 500.

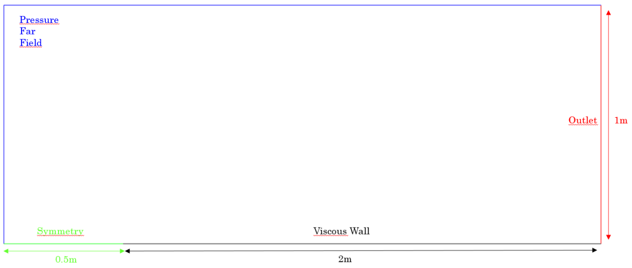

Figure 4.11: Solution domain with boundary conditions

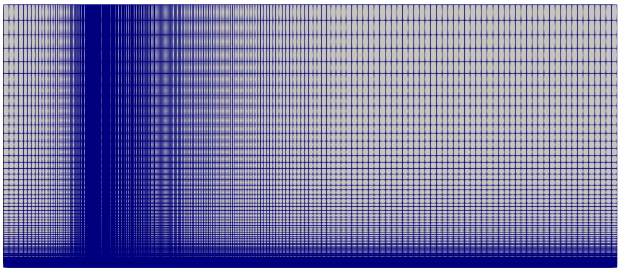

Figure 4.12: Computational domain.

Firstly, a laminar boundary layer problem is conducted to assess the abilities of the implemented methods of resolving shear layers without turbulence modelling. Computed flow conditions are given in Table 4.3. Figures 4.134.14 show the comparison of the velocity profiles (at $L = 1m$) against $\eta = \frac{y}{x}\sqrt{Re}$, and wall skin frictions of all implemented methods with the Blasius exact laminar boundary layer solutions [45].

Also, the effect of the accumulation of molecular, turbulent, and artificial viscosities in turbulent flows on the solution accuracy is tested. For this purpose, the same prob-

Table 4.3: Laminar flow conditions.

M	0.2
T_∞	300 K
p_∞	2290 Pa
Re_L	$2 * 10^5$

lem is conducted at a higher Reynolds number with the $k-\omega$ SST [46] RANS model. Turbulent flow conditions are given in Table 4.4. The original schemes and their artificial viscosity added versions are compared regarding wall skin friction. Solutions are presented in Figure 4.15 .

Table 4.4: Turbulent flow conditions

M	0.3
T_∞	288 K
p_∞	101325 Pa
Re_L	$13.9 * 10^6$

4.2.2 Results

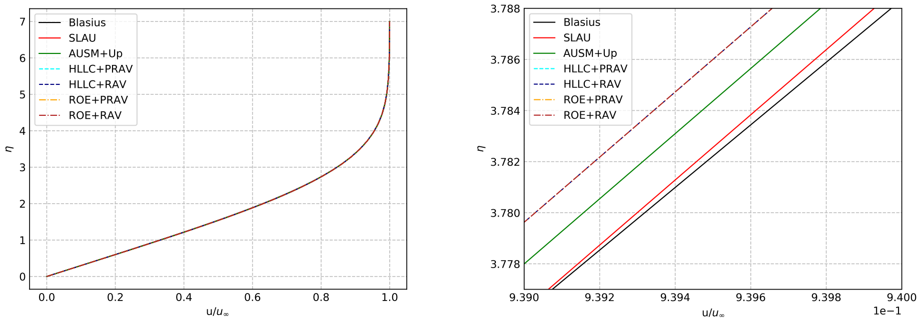

(a) Standart view.

(b) Zoomed view.

Figure 4.13: Non-dimensional velocity for the flat plate laminar boundary layer problem.

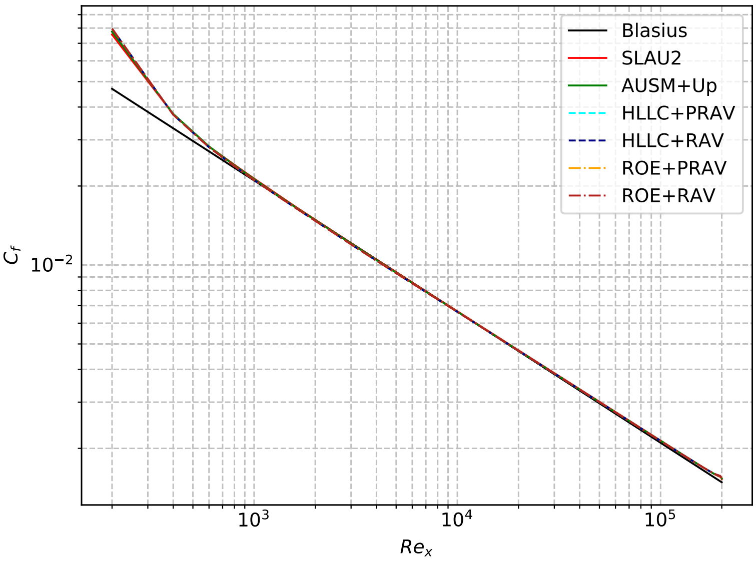

Figure 4.14: Wall skin frictions for the flat plate laminar boundary layer problem.

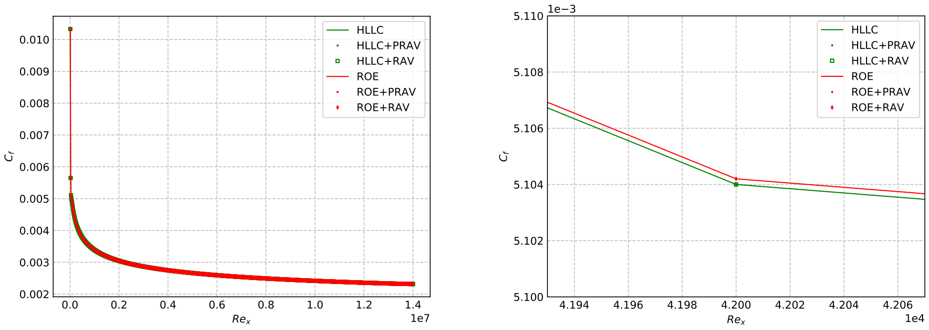

(a) Standart view.

(b) Zoomed view.

Figure 4.15: Wall skin frictions for the flat plate turbulent boundary layer problem.

All solutions, which cannot be distinguished unless examined in detail, agree very well with the Blasius solution. As expected, AUSM-type methods produce not the same but very close solutions to complete Riemann solvers Roe and HLLC. Also, artificial viscosity added schemes give identical results to classical ones in both laminar and turbulent solutions. This shows us that both Rodinov's and self-implemented dimensional parameter free shock sensors, which control artificial viscosity, work successfully. Results of that test case show that implemented methods are not only robust for capturing strong shocks but also accurate for the boundary layer calculations. Therefore, all implemented methods can be used in viscous flow problems.

4.3 Ballistic Rocket Geometry HB-2

In previous tests, it has been ensured that implemented methods are carbuncle-free and precise in boundary layer solutions. This final test compares implemented methods in terms of applicability on three-dimensional unstructured meshes and assesses their aerodynamic heating solution capabilities. For this purpose, this test case considers the hypersonic flow over the standard ballistic correlation model HB-2.

4.3.1 Problem Set-Up

Model is one of two hypersonic rocket configurations that the Supersonic Tunnel Association introduced in 1960. The HB-2 has an axisymmetric, analytical shape that consists of a sphere at the nose, cylinder at the body, and flare at the base, which is given in Figure 4.16.

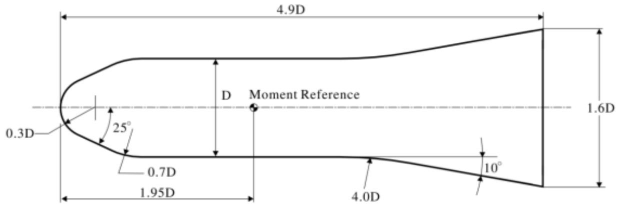

Figure 4.16: HB-2 geometry.[9]

With its simple geometry, the HB-2 geometry reduces uncertainties from the geometrical complexity. Therefore, it has great usage for experimental and numerical hypersonic test techniques validation. There are many experimental studies that investigate aerodynamic force and heating characteristics of HB-2 in hypersonic regimes. To test implemented methods' performance on three-dimensional unstructured grids static pressure distribution of the model at zero angle of attack is compared with the results of the experiments conducted by Gray and Lindsay[47] in 1964.

Three different cases with varying Mach numbers are performed to evaluate the methods at different speeds. Also, to compare the aerodynamic heating prediction capabilities of implemented methods, $\dot{q}$ distribution data of the tests performed by the Japan Aerospace Exploration Agency (JAXA) [48] are used. In order to minimize errors caused by mesh topology, analyses performed for calculating $\dot{q}$ distribution are obtained by the axisymmetric solution of the two-dimensional structured mesh. Flow properties of all conducted simulations are given in Table 4.5. While the viscous walls are considered adiabatic for the pressure distribution comparisons, it is stated as 300 K, identically to JAXA's measurement strategy, in the simulations where the heat transfer is calculated. Also, cylinder diameter D is set to 0.1 m.

Table 4.5: Flow properties for simulations.

Parameter	Case-1	Case-2	Case-3	Axis-Case
T_∞	100 K	100 K	100 K	55.3 K
p_∞	1343 Pa	943 Pa	420 Pa	74.5 Pa
M	3.99	5.05	8.04	9.59
Re_D	$0.54 * 10^6$	$0.48 * 10^6$	$0.34 * 10^6$	$0.18 * 10^6$

Two types of solution domains are generated for simulations. The first one is a two-dimensional domain that consists of a bow and a vertical line. It is generated for axisymmetric simulations. The solution domain with boundary conditions is given in Figure 4.17.

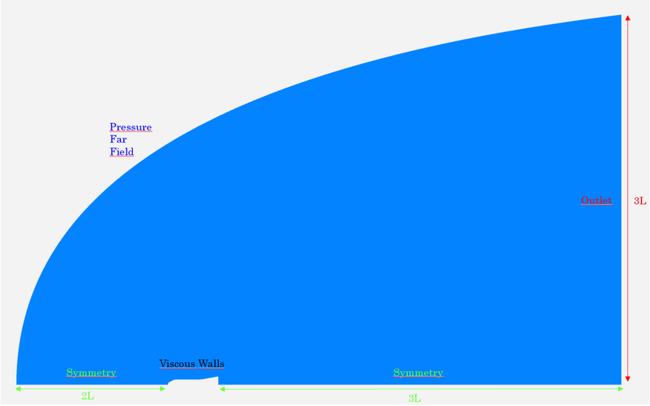

Figure 4.17: Axisymmetric domain with boundary conditions.

The computational mesh is a fine structured grid clustered toward the body with a growth factor of 1.1. First cells' y+ are taken as 0.05 to capture heat transfer under hypersonic flow conditions by directly solving the wall. Thanks to the low computational cost of the axisymmetric domain, a dense mesh is created to capture aerodynamic heating rates. Generated grid is presented in Figure4.18.

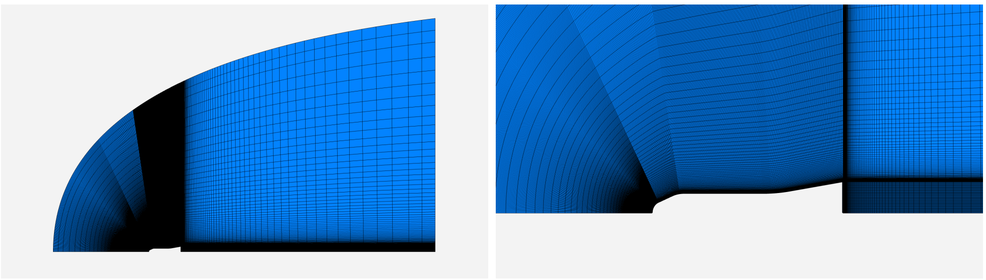

(a) Standart view.

(b) Zoomed view.

Figure 4.18: Axisymmetric computational domain.

Second domain is a semi-ellipsoid, which is generated for three-dimensional analyses. The solution domain with boundary conditions is given in Figure 4.19

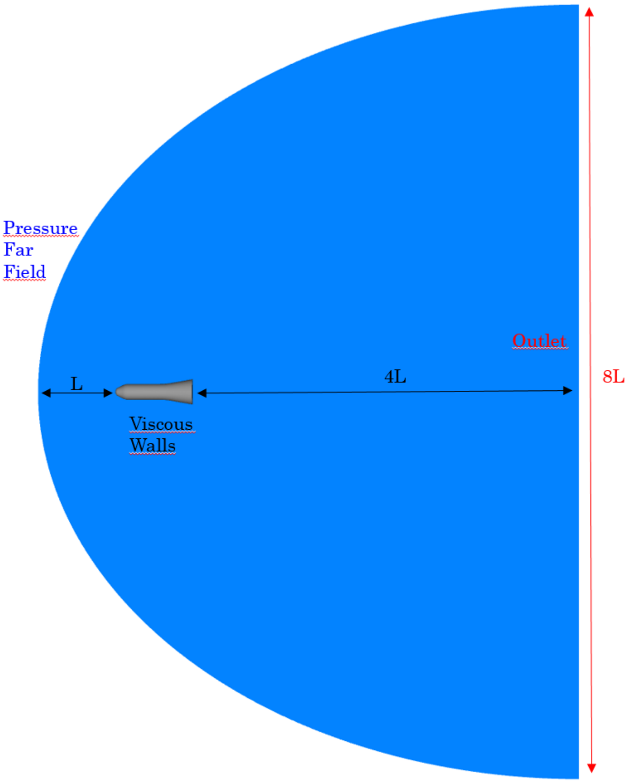

Figure 4.19: Three-dimensional domain with boundary conditions.

The solution domain is discretized with high-quality mesh to ensure high fidelity results. To obtain pressure distributions accurately, a dense, unstructured mesh is generated. Also, the boundary layer is modeled with prism cells, and a mesh independency study is carried out. To satisfactorily resolve the highly viscous boundary layer, 30 layer prism cells, which have dimensionless first layer height (y+) between 0.2 and 0.3 for different cases, are generated.

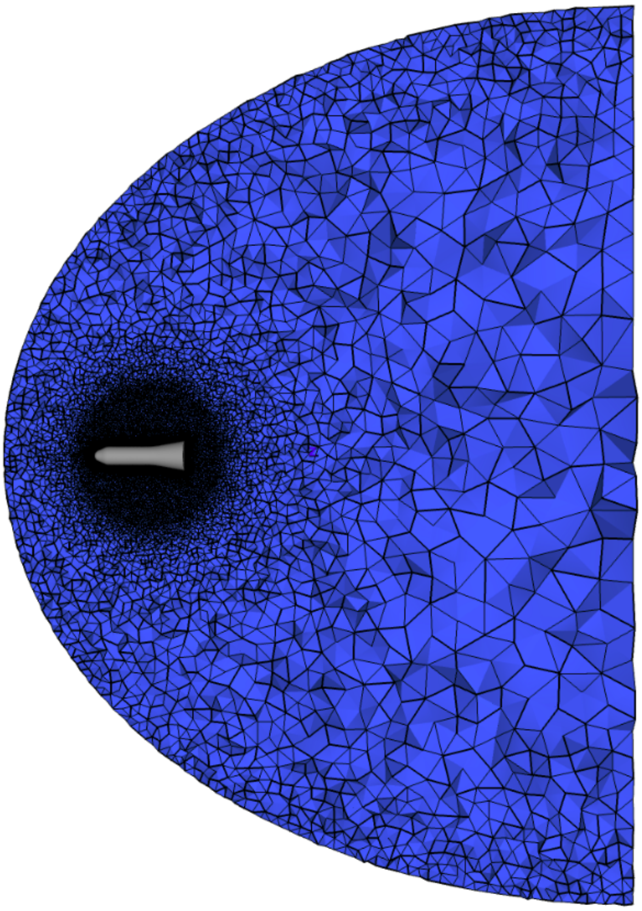

Figure 4.20: Three-dimensional computational domain.

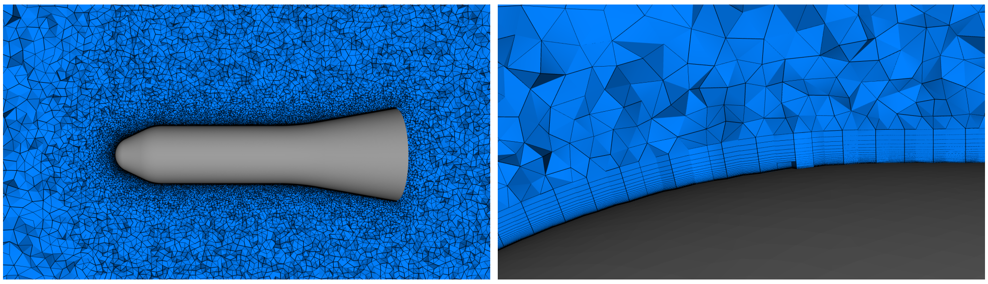

(a) Standart view.

(b) Zoomed view.

Figure 4.21: Prism layers.

Mesh independency is examined with axial force results to obtain optimum grid density with minimum spatial discretization error. This examination is carried out with the SLAU2 scheme for the case with the highest Mach number(Case-3). Results are given in Figure 4.22. As seen, axial force do not change notably(less than %0.001) even if we increase the total number of cells after 12.5 million. Thus, this mesh size is chosen and used in three-dimensional analyses.

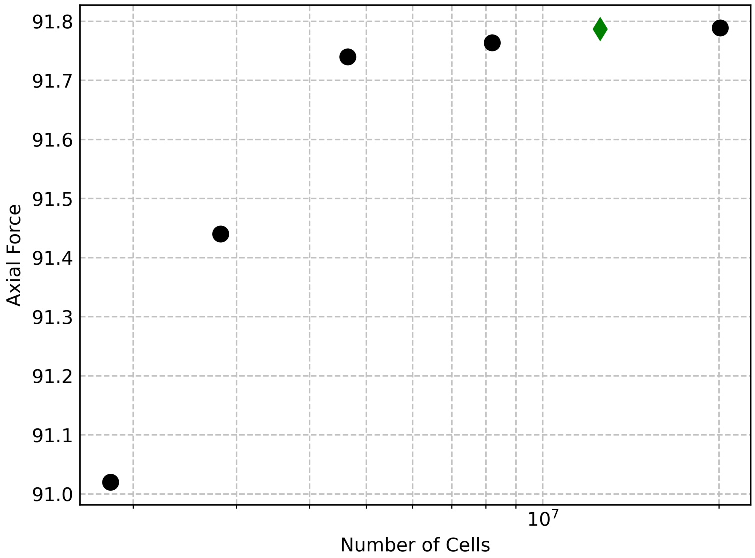

Figure 4.22: Axial force for different number of cells.

Flow simulations are conducted at given conditions for all implemented methods. Obtained results are compared with the experimental results. All analyses are performed with second-order spatial accuracy. Although in Reference [49], it is suggested to assume the flow field as laminar due to low Reynold Numbers for HB-2 calculations, Reference [50] mentioned that a proper turbulence model increases the accuracy of hypersonic flow calculations. Therefore, the $k - \omega$ SST [46] turbulence model is employed for all cases to resolve complex flow structures more accurately and stably.

All analyses are iterated until residuals drop at least two orders and stop decreasing. The convergence history for each case is given in Figures 4.23, 4.24.

CFL numbers and iteration numbers used to conduct simulations are given in Table4.6.

Table 4.6: Simulation parameters .

Parameter	Case-1	Case-2	Case-3	Axis-Case
CFL	0.5	0.3	0.2	0.1
Iteration	15000	15000	15000	100000

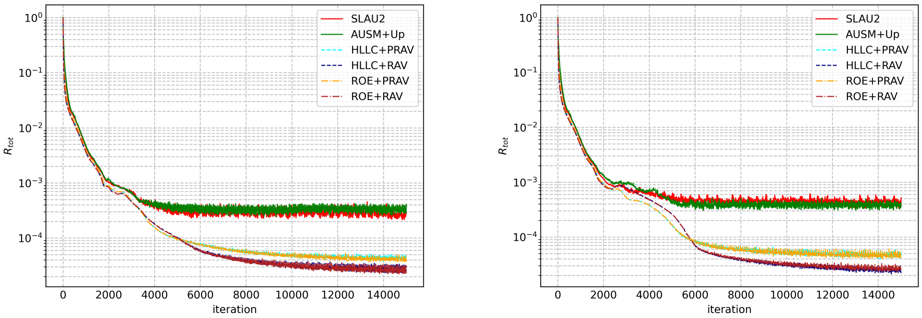

(a) Case-1 (b) Case-2

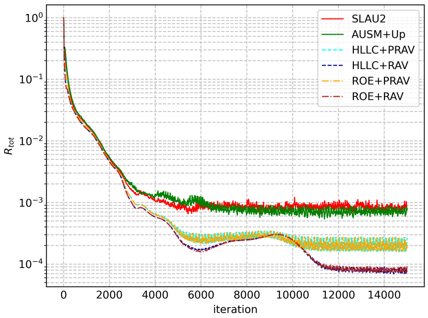

(c) Case-3

Figure 4.23: Convergence history of three-dimensional analyses.

Figures 4.23, 4.24 show that all implemented methods display well-behaved convergence histories. Schemes from AUSM family showed similar convergence performance for all cases. Also, RAV and PRAV methods generated almost identical residual histories within themselves with ROE and HLLC schemes. This shows us that artificial viscosity has a dominant effect on the solution's convergence performance, regardless of the Riemann solver to which it is added. Although the drop rates of residuals are similar for all methods, artificial viscosity based methods, especially PRAV, are decreased residuals to lower orders than AUSM type schemes. In this way,

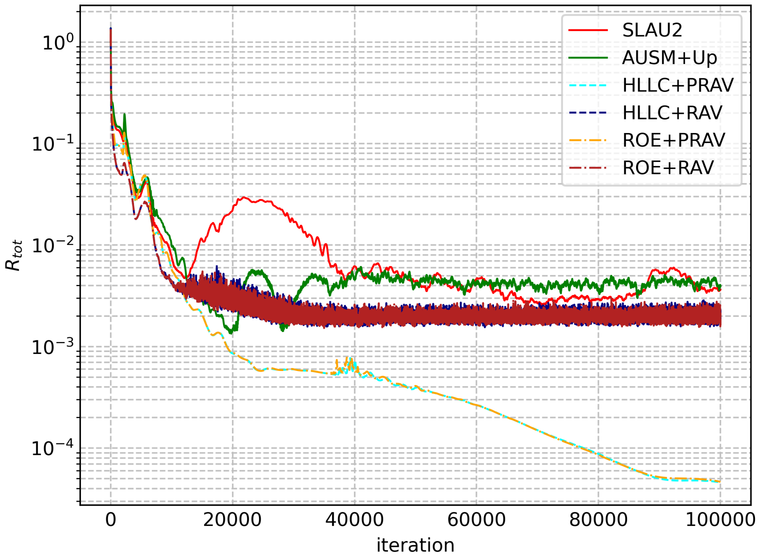

Figure 4.24: Convergence history of axisymmetric analyses.

they generated more stable solutions.

Artificial viscosity,μ_{AV}, contours of ROE+RAV and ROE+PRAV methods for Case-3 are presented in Figure 4.25 to examine whether methods affect the solutio domain while producing these stable solutions. As seen from the contours, the RAV method produces more artificial viscosity than the PRAV method due to its shock sensor with dimensional parameters. This shows us dimensional-parameter free PRAV methodology affects the solution domain less than RAV method for solutions with similar convergence performance.

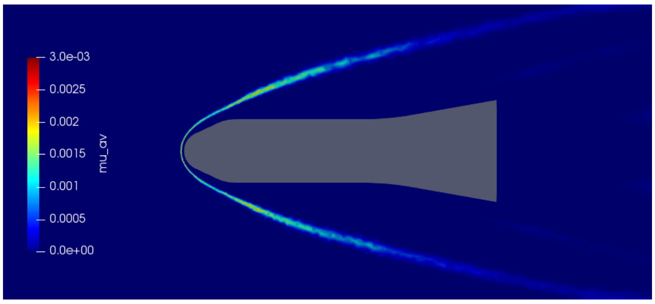

(a) ROE+PRAV

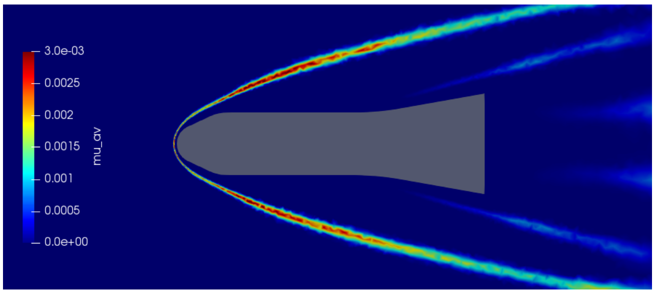

(b) ROE+RAV

Figure 4.25: μ_{AV} contours of artificial viscosity methods for Case-3.

Also, velocity profiles of ROE+RAV and ROE+PRAV methods at $x = 0.2m$ for the same case compared with SLAU2 solutions in Figure 4.26. From the similarity of results, it has been ensured that both artificial viscosity based methods do not affect boundary layer solutions, as expected.

4.3.2 Results

In Figures 4.27, 4.28, 4.29 the pressure ratio along the HB-2 model wall for Cases 1,2, and 3 are shown. As given in the figures, the computational results are not exact but in good agreement with experimental measurements for all Mach numbers. While two pressure drops, related to the two expanding curves in the fore-body, are captured excellently by all methods, they disagree with experiment a little near the joint of the body and flare for all cases. These mismatches can be related to numerical errors arising from using unstructured meshes or vortex effects in that region.

The only difference between the implemented methods, which show almost identical compatibility for all cases, is that highly stable artificial viscosity based methods

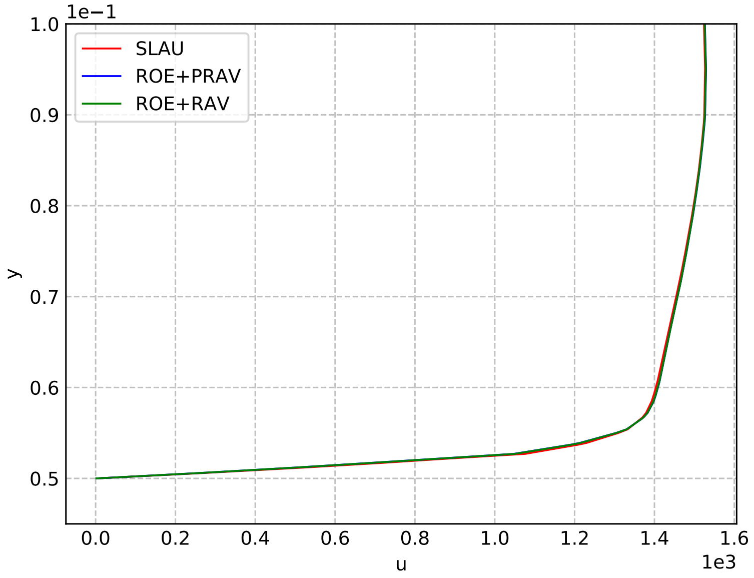

Figure 4.26: Velocity profiles for the HB-2 boundary layer.

produce smooth distributions, whereas AUSM schemes exhibit slight oscillatory behavior, as expected.

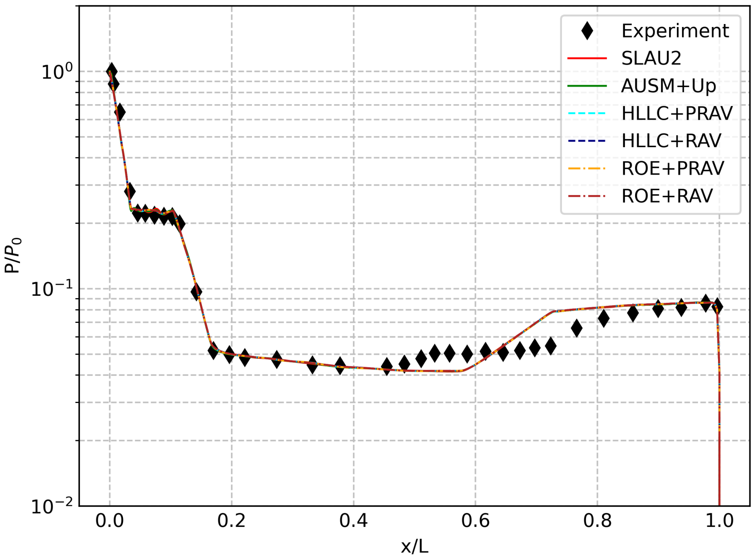

(a) Standart view.

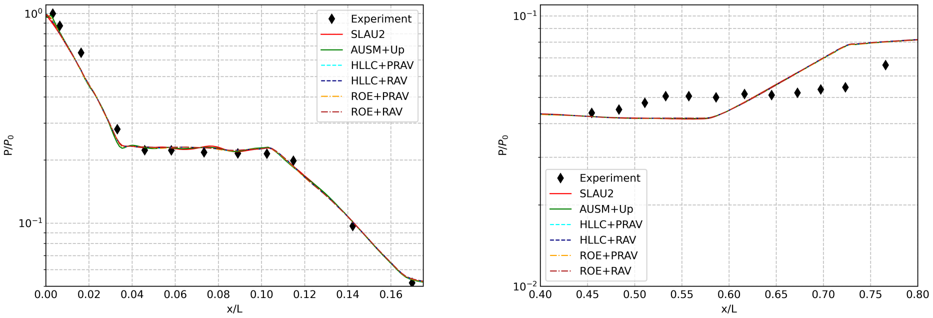

(b) Zoomed view 1.

(c) Zoomed view 2.

Figure 4.27: Pressure distribution prediction over model surface for Case-1.

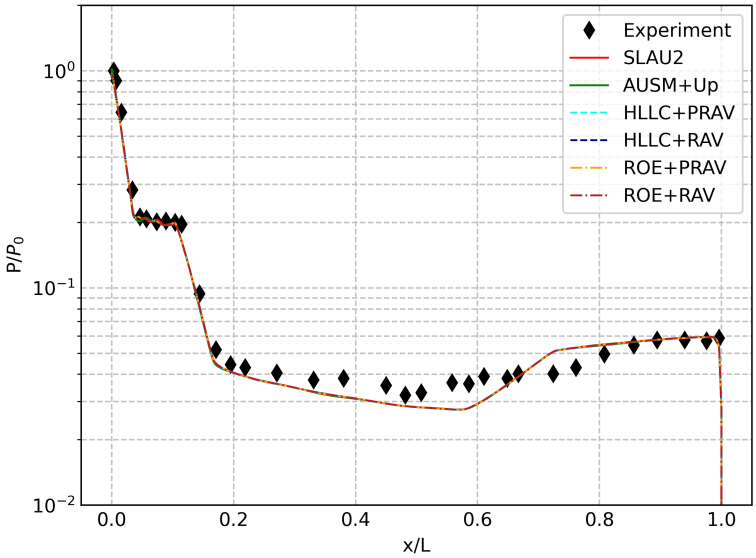

(a) Standart view.

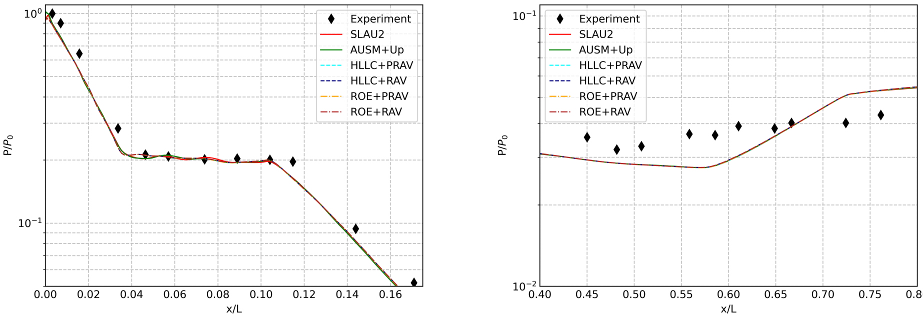

(b) Zoomed view 1.

(c) Zoomed view 2.

Figure 4.28: Pressure distribution prediction over model surface for Case-2.

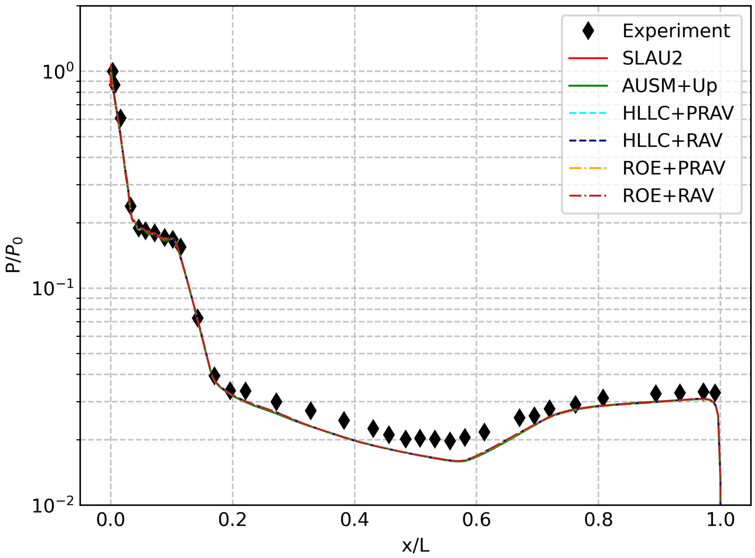

(a) Standart view.

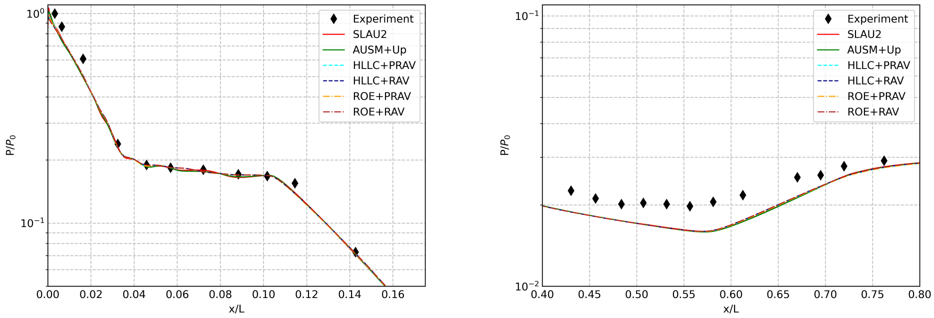

(b) Zoomed view 1.

(c) Zoomed view 2.

Figure 4.29: Pressure distribution prediction over model surface for Case-3.

Figure 4.30 shows the comparison of numerical heat transfer predictions obtained from the solution of the axisymmetric model with the experimental results. Similar to pressure distribution comparisons, numerical predictions of $\dot{q}$ of all implemented methods are compatible with JAXA's experimental measurements. However, that case reveals methods' differences more clearly. For example, while artificial viscosity based methods maintain their smoothness, AUSM schemes produce more visible oscillating results than pressure distribution. Also, the PRAV methodology generates more compatible results with experimental data than RAV, especially in the flare region. This shows us RAV method can cause distortions in the solution domain due to its excessive viscosity production. In contrast, PRAV preserves its accuracy in the entire domain for solutions with the same stability.

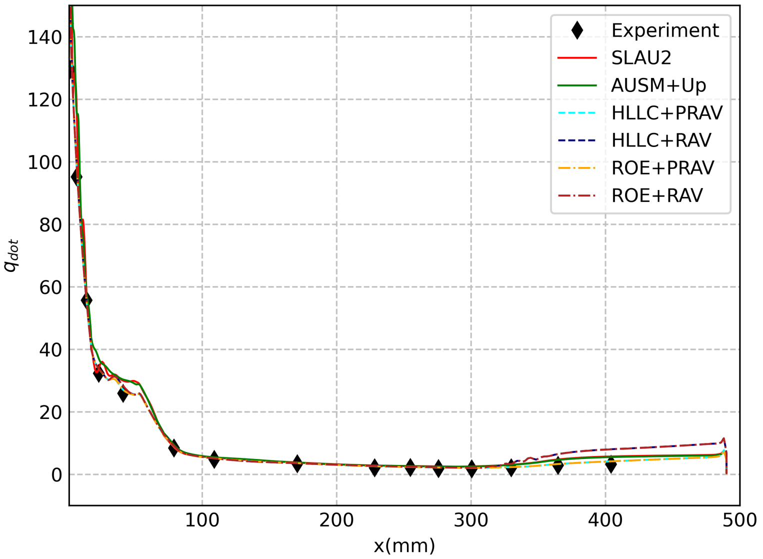

(a) Standart view.

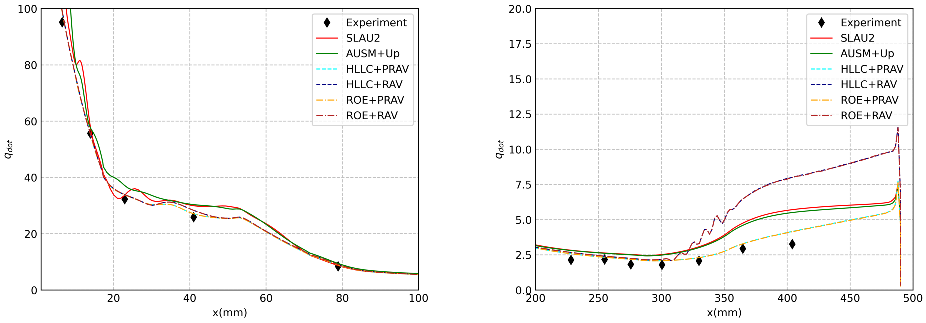

(b) Zoomed view 1.

(c) Zoomed view 2.

Figure 4.30: Heat transfer prediction over model surface for axisymmetric case.

CHAPTER 5

CONCLUSION AND FUTURE WORK

5.1 Conclusions

In this study, the performances of three different shock-capturing methodologies are analyzed for viscous flow calculations in hypersonic regimes. The first methodology is based on all-speed AUSM family schemes. Prominent SLAU2 and AUSM+up are implemented into the in-house CFD solver. The second method is based on an explicit diffusion term based on Von Neumann and Richtmyer's artificial viscosity. ROE+RAV, and HLLC+RAV schemes are generated by adding that diffusion to the Roe and HLLC complete Reimann solvers. This artificial diffusion must only be introduced in shock layers, without any effect in the flow regions without discontinuities. For this, the shock sensor has a critical role in this methodology. However, the shock sensor of RAV method can be case-dependent because of its dimensional parameters. Therefore, a final methodology, which combines the artificial viscosity of RAV with a pressure-ratio based shock sensor, is proposed. ROE+PRAV, and HLLC+PRAV schemes are generated with this methodology.

All methods are validated by several numerical test cases in Chapter 4. The main focus of the numerical examples is understanding the different shock-capturing techniques and the detailed comparison between them. For this purpose, firstly, an inviscid hypersonic flow over blunt body problem is used to demonstrate the need for shock-capturing when low-dissipative Reimann solvers are used. This test also shows the capability of the implemented methods to solve problems with strong shocks. Then, a flat plate example is conducted to understand the boundary-layer resolution capabilities of these methods. Finally, in the last test case, the implemented methods' performances are compared for calculations of three-dimensional configurations and heat transfer prediction with the HB-2 model.

Results show that both AUSM family schemes and artificial viscosity based methods are highly resistant to shock anomalies and have low diffusion at low speeds. Also, both are applicable to three-dimensional unstructured grids. When compared with each other, they have benefits as well as drawbacks relative to each other. Artificial viscosity based methods produce much more stable and smoother solutions with better convergence performance than AUSM family schemes. However, as a critical deficiency, they have a user-defined parameter, C_{AV},that might need recalibration for different solutions. On the other hand, their simple, easily extendable and almost user-defined parameter free structures of AUSM family schemes provide great advantages.

When AUSM family schemes are compared among themselves, SLAU2 is advantageous over AUSM+up by its user-defined parameter free formulation and more stable characteristics. Also, the self-generated PRAV shock sensor is proved to be more accurate than RAV sensor, especially for heat transfer predictions, with less impact on the overall domain.

5.2 Future Works

Implicit solution of numerical problems provides higher stability with larger time steps than an explicit ones. However, the derivatives of the interface fluxes, which are hard to evalute exactly for complex flux functions like AUSM family schemes, are needed for the implicit formulation. Generally, CFD solvers, like our in-house solver, employ approximate Roe jacobian regardless of used flux function for an implicit solution. However, when possible, an exact jacobian of the used flux function is preferred because it is more efficient. Therefore, exact jacobians of AUSM+up and SLAU2, which are constructed by automated differentiation technique [51], can be implemented to enhance stability and accuracy results.

Although PRAV shock sensor produces accurate and stable results in tests, improvements can be made, especially for decreasing dependency on C_{AV} parameter and make it usable for wide range of applications.

Implemented methods are tested in this study on simple models without the angle of attack or side-slip angles. Thus, the physical complexity of the problem simulated can be increased. Flow problems remain to be investigated by the implemented methods' performance on highly turbulent or involving complex structures like shock-shock or shock-boundary layer interactions. Furthermore, chemical reactions and material ablation can be added to the simulated problems.

REFERENCES

[1] J. D. Anderson, *Hypersonic and high temperature gas dynamics*. Aiaa, 2000.

[2] M. Pandolfi and D. D'Ambrosio, "Numerical instabilities in upwind methods: analysis and cures for the "carbuncle" phenomenon," *Journal of Computational Physics*, vol. 166, no. 2, pp. 271–301, 2001.

[3] E. F. Toro, *Riemann solvers and numerical methods for fluid dynamics: a practical introduction*. Springer Science & Business Media, 2013.

[4] C. Hirth, "Numerical computation of internal and external flows," *Computational methods for inviscid and viscous flows*, vol. 2, 1990.

[5] E. F. Toro, *The Riemann problem: solvers and numerical fluxes*, vol. 17. Elsevier, 2016.

[6] K. Kitamura, *Advancement of Shock Capturing Computational Fluid Dynamics Methods*, vol. 136. Springer, 2020.

[7] S.-s. Chen, C. Yan, B.-x. Lin, L.-y. Liu, and J. Yu, "Affordable shock-stable item for Godunov-type schemes against carbuncle phenomenon," *Journal of Computational Physics*, vol. 373, pp. 662–672, 2018.

[8] S. Henderson and J. Menart, "Grid study on blunt bodies with the carbuncle phenomenon," in *39th AIAA thermophysics conference*, p. 3904, 2007.

[9] A. Kryuchkova, "Numerical simulation of a hypersonic flow over HB-2 model using UST3D programming code," in *Journal of Physics: Conference Series*, vol. 1250, p. 012010, IOP Publishing, 2019.

[10] G. E. Barter, "Shock capturing with PDE-based artificial viscosity for an adaptive, higher-order discontinuous Galerkin finite element method," tech. rep., MASSACHUSETTS INST OF TECH CAMBRIDGE DEPT OF AERONAUTICS AND ASTRONAUTICS, 2008.

[11] K. Peery and S. Imlay, "Blunt-body flow simulations," in *24th Joint Propulsion Conference*, p. 2904, 1988.

[12] J. J. Quirk, "A contribution to the great Riemann solver debate," in *Upwind and High-Resolution Schemes*, pp. 550–569, Springer, 1997.

[13] A. S. Mohamed Sherif, "Shock-capturing techniques for Euler equations in the framework of Hybridizable Discontinuous Galerkin," Master's thesis, Universitat Politècnica de Catalunya, 2018.

[14] J. VonNeumann and R. D. Richtmyer, "A method for the numerical calculation of hydrodynamic shocks," *Journal of applied physics*, vol. 21, no. 3, pp. 232–237, 1950.

[15] P. D. Lax, "Weak solutions of nonlinear hyperbolic equations and their numerical computation," *Communications on pure and applied mathematics*, vol. 7, no. 1, pp. 159–193, 1954.

[16] S. Godunov and I. Bohachevsky, "Finite difference method for numerical computation of discontinuous solutions of the equations of fluid dynamics," *Matematičeskij sbornik*, vol. 47, no. 3, pp. 271–306, 1959.

[17] J. L. Steger and R. Warming, "Flux vector splitting of the inviscid gasdynamic equations with application to finite-difference methods," *Journal of computational physics*, vol. 40, no. 2, pp. 263–293, 1981.

[18] B. v. Leer, "Flux-vector splitting for the Euler equation," in *Upwind and high-resolution schemes*, pp. 80–89, Springer, 1997.

[19] A. Harten, "High resolution schemes for hyperbolic conservation laws," *Journal of computational physics*, vol. 135, no. 2, pp. 260–278, 1997.

[20] B. Einfeldt, "On Godunov-type methods for gas dynamics," *SIAM Journal on numerical analysis*, vol. 25, no. 2, pp. 294–318, 1988.

[21] P. L. Roe, "Approximate Riemann solvers, parameter vectors, and difference schemes," *Journal of computational physics*, vol. 43, no. 2, pp. 357–372, 1981.

[22] E. F. Toro, M. Spruce, and W. Speares, "Restoration of the contact surface in the HLL-Riemann solver," *Shock waves*, vol. 4, no. 1, pp. 25–34, 1994.

[23] D. Wang, X. Deng, G. Wang, and Y. Dong, "Developing a hybrid flux function suitable for hypersonic flow simulation with high-order methods," *International Journal for Numerical Methods in Fluids*, vol. 81, no. 5, pp. 309–327, 2016.

[24] Z. Shen, W. Yan, and G. Yuan, "A robust HLLC-type Riemann solver for strong shock," *Journal of Computational Physics*, vol. 309, pp. 185–206, 2016.

[25] W. Xie, Z. Tian, Y. Zhang, H. Yu, and W. Ren, "A unified construction of all-speed HLL-type schemes for hypersonic heating computations," *Computers & Fluids*, vol. 233, p. 105215, 2022.

[26] S. Simon and J. Mandal, "A cure for numerical shock instability in HLLC Riemann solver using antidiffusion control," *Computers & Fluids*, vol. 174, pp. 144–166, 2018.

[27] S. Simon and J. Mandal, "A simple cure for numerical shock instability in the HLLC Riemann solver," *Journal of Computational Physics*, vol. 378, pp. 477–496, 2019.

[28] S. Simon and J. Mandal, "Strategies to cure numerical shock instability in the HLLEM Riemann solver," *International Journal for Numerical Methods in Fluids*, vol. 89, no. 12, pp. 533–569, 2019.

[29] M.-S. Liou and C. J. Steffen Jr, "A new flux splitting scheme," *Journal of Computational physics*, vol. 107, no. 1, pp. 23–39, 1993.

[30] M.-S. Liou, "A further development of the AUSM+ scheme towards robust and accurate solutions for all speeds," in *16th AIAA Computational Fluid Dynamics Conference*, p. 4116, 2003.

[31] E. Shima and K. Kitamura, "Parameter-free simple low-dissipation AUSM-family scheme for all speeds," *AIAA journal*, vol. 49, no. 8, pp. 1693–1709, 2011.

[32] K. Kitamura and E. Shima, "Towards shock-stable and accurate hypersonic heating computations: A new pressure flux for AUSM-family schemes," *Journal of Computational Physics*, vol. 245, pp. 62–83, 2013.

[33] K. Kitamura and E. Shima, "AUSM-like expression of HLLC and its all-speed extension," *International Journal for Numerical Methods in Fluids*, vol. 92, no. 4, pp. 246–265, 2020.

[34] A. V. Rodionov, "Artificial viscosity in Godunov-type schemes to cure the carbuncle phenomenon," *Journal of Computational Physics*, vol. 345, pp. 308–329, 2017.

[35] A. V. Rodionov, "Artificial viscosity to cure the carbuncle phenomenon: The three-dimensional case," *Journal of Computational Physics*, vol. 361, pp. 50–55, 2018.

[36] A. V. Rodionov, "Artificial viscosity to cure the shock instability in high-order Godunov-type schemes," *Computers & Fluids*, vol. 190, pp. 77–97, 2019.

[37] A. V. Rodionov, "Simplified artificial viscosity approach for curing the shock instability," *Computers & Fluids*, vol. 219, p. 104873, 2021.

[38] J. Blazek, *Computational fluid dynamics: principles and applications*. Butterworth-Heinemann, 2015.

[39] C. B. Laney, *Computational gasdynamics*. Cambridge university press, 1998.

[40] P. W. McDonald, *The computation of transonic flow through two-dimensional gas turbine cascades*, vol. 79825. American Society of Mechanical Engineers, 1971.

[41] R. MacCormack and A. Paullay, "Computational efficiency achieved by time splitting of finite difference operators," in *10th aerospace sciences meeting*, p. 154, 1972.

[42] M.-S. Liou, "A sequel to AUSM: Ausm+," *Journal of computational Physics*, vol. 129, no. 2, pp. 364–382, 1996.

[43] N. Fleischmann, S. Adami, and N. A. Adams, "A shock-stable modification of the HLLC Riemann solver with reduced numerical dissipation," *Journal of Computational Physics*, vol. 423, p. 109762, 2020.

[44] "Nasa turbulence modeling resource."

[45] H. Schlichting and K. Gersten, "Boundary—layer equations in plane flow; plate boundary layer," in *Boundary-layer theory*, pp. 145–164, Springer, 2000.

[46] F. Menter, "Zonal two equation kw turbulence models for aerodynamic flows," in *23rd fluid dynamics, plasmadynamics, and lasers conference*, p. 2906, 1993.

[47] J. D. Gray, "Summary report on aerodynamic characteristics of standard models HB-1 and HB-2," tech. rep., ARNOLD ENGINEERING DEVELOPMENT CENTER ARNOLD AFB TN, 1964.

[48] S. Kuchi-Ishi, S. Watanabe, S. Nagai, S. Tsuda, T. Koyama, N. Hirabayashi, H. Sekine, and K. Hozumi, "Comparative force/heat flux measurements between JAXA hypersonic test facilities using standard model hb-2 (part 1: 1.27 m hypersonic wind tunnel results)," *JAXA research and development report, Japan Aerospace Exploration Agency, Japan*, 2005.

[49] F. Mohammadifard, M. Karami, and M. Heidari, "Investigation of flow field in a typical hypersonic wind tunnel over a standard mode," *Journal of applied fluid mechanics*, vol. 6, no. 4, pp. 529–536, 2013.

[50] M. P. Pajčin, A. M. Simonović, T. D. Ivanov, D. M. Komarov, and S. N. Stupar, "Numerical analysis of a hypersonic turbulent and laminar flow using a commercial CFD solver," *Thermal Science*, vol. 21, no. suppl. 3, pp. 795–807, 2017.

[51] C. C. Margossian, "A review of automatic differentiation and its efficient implementation," *Wiley interdisciplinary reviews: data mining and knowledge discovery*, vol. 9, no. 4, p. e1305, 2019.